Aalto University School of Electrical Engineering
Department of Micro- and Nanosciences
Master's Programme in Micro- and Nanotechnology

Martin Aurientis

Interdigitated Back Contact n-Type Solar Cell with Black Silicon Anti-Reflecting Layer: Simulations and Experiments

Thesis submitted in partial fulfilment of the requirements for the degree of Master of Science in Technology.

Espoo 27.06.2014

Supervisor: Professor Hele Savin

Instructors: Natalia Lebedeva, Guillaume von Gastrow

AALTO UNIVERSITY
SCHOOL OF ELECTRICAL ENGINEERING

ABSTRACT OF THE
MASTER'S THESIS

Author: Martin Aurientis

Title: Interdigitated Back Contact n-Type Solar Cell with black-Silicon Anti-Reflecting Layer: Simulations and Experiments

Date: 30.06.2014 | Language: English | Number of pages: 8 + 56 +9

Department of Micro and Nanosciences
Professorship: Micro- and Nanoelectronics

Code: S-69

Supervisor: Professor Hele Savin

Instructor: Natalia Lebedeva and Guillaume von Gastrow

Abstract:
In this work, we have processed as a reference n-type IBC cells with random pyramids on high quality float-zone silicon wafer. The front surface is passivated with Al_2O_3 grown by atomic layer deposition. The same structure is simulated with the software Silvaco ATLAS. The simulated IV-characteristic fits the experimental curve in the dark and under AM1.5G with a relative error below 1%.

Previous measurements on minority carrier lifetime experiments on black silicon samples passivated with 20nm Al_2O_3 layer have resulted in an effective surface recombination velocity below 5 cm/s. This value was used to simulate IBC cells with black silicon by adjusting the above-mentioned ATLAS model in order to see the impact of black silicon on the solar cell efficiency.

The results show an increase in short-circuit current (Isc) of 6mA and efficiency of 0.3% at normal incidence. Simulation reveals that a lower front surface recombination velocity would not significantly increase the efficiency of the cell. Furthermore, the simulations reveal that the emitter passivation is a critical parameter to increase further the efficiency of the cell.

Keywords: solar cell, IBC, BC-BJ, black silicon, ATLAS, Silvaco, simulation.

Acknowledgements

First, I would like to thank Professor Hele Savin for giving me the opportunity to work in the Electron Physic research group and for her supervising.

I would like to especially thank Guillaume Von Gastrow and Natalia Lebedeva for helping me and giving me precious advices throughout my master's thesis.

Finally, I would like to thank Professor Pablo Ortega and Eric Calle for their help and welcome at the polytechnic university of Barcelona.

Contents

Nomenclature

Abbreviations

AM0	Air Mass zero spectrum
AM1	Air Mass 1 spectrum
AM1.5	Air Mass 1.5 spectrum
AR	Anti-Reflection
BC	Back-Contact
BSF	Back Surface Field
BJ	Back-Junction
CVP	Concentrating Photovoltaic
FF	Fill-Factor
FSF	Front-Surface-Field
IBC	Interdigitated-Back-Contact
Mcz	Magnetic Czochralski
MEMS	Microelectromechanical systems
PC	Point-Contact
QSS	Quasi-steady-state
RIE	Reactive Ion Etching
SC	Solar Cell
SRH	Shockley-Read-Hall

ALTAS Abbreviations

AUGER	Auger Recombination
BGN	Band-gap narrowing
CCSMOD	Carrier-carrier scattering
CONSRH	Concentration dependence of Shockley-Read-Hall recombination
FERMI	Fermi-Dirac distribution
FLDMOD	Parallel electric field dependence
SRH	Shockley-Read-Hall recombination

Simulations symbols

BSF	Back-surface-field
BSF+	Selective back-surface-field
BSFHighNPeak	BSF+ peak concentration
BSFNPeak	BSF peak concentration
bulkRes	Bulk resistivity
EmitterNPeak	Emitter peak concentration
Gap	Gap between the back-surface-field and the emitter

$Gap_{electrode}$	Gap between the electrodes
SBackBSF	Surface recombination parameters at the BSF surface
SBackBSFHigh	Surface recombination parameters at the BSF+ surface
SBackEmitter	Surface recombination parameters at the emitter surface
SFront	Surface recombination parameters at the front surface
SNBack	Electron surface recombination parameters at the gap surface
SPBack	Hole surface recombination parameters at the gap surface
tau	CONSRH electron and hole lifetime
VEletrode	Surface recombination parameters at electrode contacts
w_{BSF}	Width of the back-surface-field
w_{BSF+}	Width of the selective back-surface-field
$w_{electrode}$	Width of electrode contact
x_{max}	Pitch of the cell
y_{BSF}	Back-surface-field depth
y_{BSF+}	Selective back-surface-field depth
$y_{emitter}$	Depth of the pn-junction
y_{max}	Thickness of the cell

Symbols

A	Cross section area of a pn-junction
C_n	Auger coefficient for electrons
C_p	Auger coefficient for holes
C_{n_LLI}	Auger coefficient for electrons at low level of injection
C_{p_LLI}	Auger coefficient for holes at low level of injection
C_{HLI}	Auger coefficient at high level of injection
E_c	Conduction band energy
E_t	Trap energy
E_v	Valence band energy
G_L	Photo-generation rate
I	Current
I_{SC}	Short-Circuit Current
I_m	Maximum power Current
J_e	Electrons current density
J_h	Holes current density
n	Electron density
n_0	Minority carrier density under thermo-dynamical equilibrium
p	Hole density
q	Elementary charge
Q_F	Surface charge density
R_{SH}	Shunt Resistance
R_S	Series Resistance
S_{eff}	Effective surface recombination velocity
S_{eff_front}	Effective front surface recombination velocity

S_{eff_rear}	Effective rear surface recombination velocity
S_n	Surface recombination velocity of electrons
S_p	Surface recombination velocity of holes
S_{Front}	Front surface recombination velocity
S_{Rear}	Rear surface recombination velocity
τ_{Auger}	Auger lifetime
τ_{Bulk}	Bulk lifetime
τ_{Rad}	Radiative lifetime
τ_{SRH}	Shockley-Read-Hall lifetime
τ_{n0}	Shockley-Read-Hall electrons lifetime
τ_{p0}	Shockley-Read-Hall holes lifetime
U	Recombination rate
U_{Auger}	Auger recombination rate
U_{Bulk}	Bulk recombination rate
U_{Rad}	Radiative recombination rate
U_s	Surface recombination rate
U_{SRH}	Shockley-Read-Hall recombination rate
V	Voltage
V_{OC}	Open-Circuit Voltage
V_m	Maximum power Voltage
w	Wafer thickness
η	Efficiency
Δn	Excess minority carrier density
Δn_S	Excess minority carrier density at the surface
$\Delta\sigma$	Average excess conductance
μ_n	Electron mobility
μ_p	Hole mobility
δ	Space charge region thickness

Introduction

Every hour, the total solar energy reaching the surface of Earth is approximately equal to the human civilisation consumption in one year. This huge potential makes solar cell technology very promising to overcome world energy issues and global warming. Moreover, this technology is very useful to bring energy in isolated areas (space, islands…).

The principal part of any solar cell is a pn-junction. The pn-junction separates the two main areas of the cell: the emitter and the base. Each area is connected to an electrode to collect the produced photocurrent.

Conventional silicon solar cells have a front-side contacted emitter. One issue of this design is that the emitter electrode reflects a large part of the incoming light. Interdigitated-back-contacted back-junction (IBC or BC-BJ) silicon solar cells, on the other hand, have both the complete metallization and the active diffused regions of both polarities on the backside. Nowadays, this new design has demonstrated world-record efficiencies in production over one sun, both on cell and module levels [1].

At the same time, silicon surface texturing has raised a lot of interest in photovoltaic applications. By texturing nano-spikes or “grass” at the surface, the incoming light is trapped in the material and the silicon turns black. The very low reflectivity of this black-silicon is a significant advantage for solar cells.

Combining IBC design with black-silicon anti-reflection layer could potentially bring the efficiency of a solar cell to a higher level. However, the high density of defects at the black-silicon surface makes this combination difficult to perform. Until now, the maximum efficiency of a silicon solar cell with black-silicon on the front side was 18.7 [2].

By depositing an aluminium oxide layer on the black-silicon, it is possible to reduce the density of defects and, at the same time, reduce the impact of those defects on the solar cell [3]. This phenomenon is called surface passivation.

In the frame of this thesis, we study the combination of IBC design and black-silicon surface passivated with aluminium oxide. The structure was modeled using Silvaco ATLAS software and compared to experimental cells for the purpose of evaluating the model. After model verification, the impacts of different parameters on the solar cell performance have been studied.

I. Theory of solar cells

A solar cell is a device that converts sunlight directly into electricity through the photovoltaic effect. The first solar cells were pn-junction fabricated from silicon at Bell Laboratories in 1954 by Chapin, Fueller and Pearson. The cells were diode-like giving an efficiency of 6% [4]. Over the time, there have been substantial improvements in silicon solar cell performance. Nowadays, the highest independently confirmed efficiency is around 25% under the global AM1.5 spectrum (1000W/m^2) [1].

1 Current-Voltage characteristics

The principal part of any solar cell is pn-junction. When it is illuminated by light with proper wavelength (photon energy is larger than the bandgap of the semiconductor constituting the p-n junction), electron-hole pairs are generated. In the depletion region of the p-n junction, photo-generated electrons and holes move under the influence of the built-in potential towards n and p sides respectively, thus contributing to the reverse current of the p-n junction. This light-generated current can be included into the conventional equation of the p-n junction, giving the current-voltage equation of the solar cell:

$$I = I_0 * \left(e^{\frac{qV}{kT}} - 1\right) - I_L \qquad \textbf{Equation I.1}$$

Figure 1(a) depicts the IV-curve of a solar cell in the dark and under illumination. As the solar cell is a current generator, the convention is to inverse the y-axis as in Figure 1(b). The power generated is also depicted in Figure 1 (b).

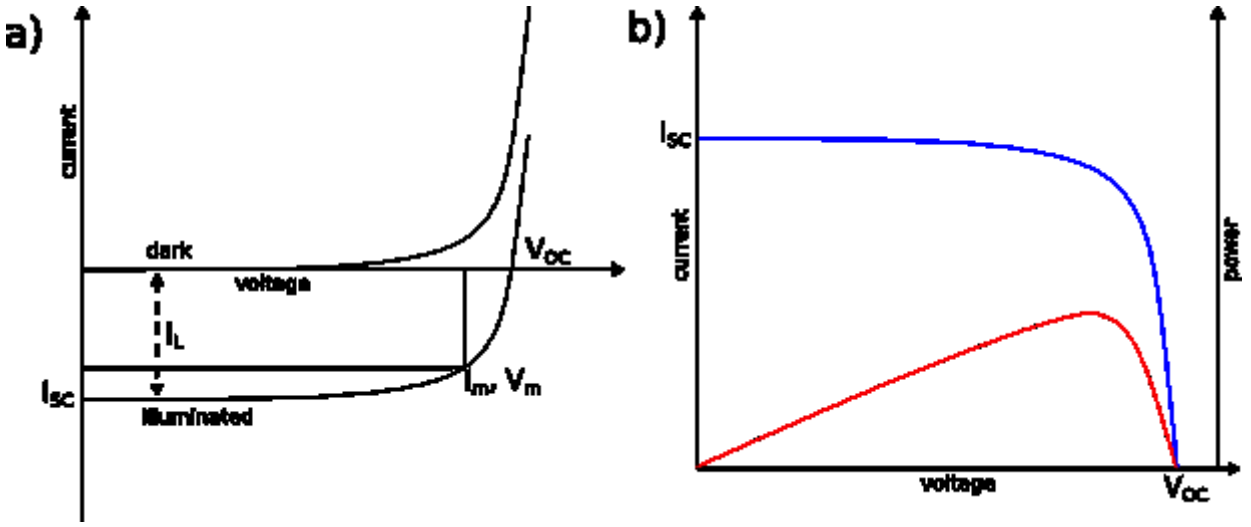

Figure 1 (a) *IV-curves of the p-n junction in the dark and under illumination. (b) IV-curves of the solar cell as they are generally presented – inverted with respect to the voltage axis (blue line) and the output power P=I*V (red line) versus voltage curve.*

The main characteristics of the particular solar cell are short circuit current I_{sc}, open-circuit voltage V_{oc}, fill factor FF and power conversion efficiency η.

- **Short circuit current** I_{sc} corresponds to the zero applied voltage and is equal to the light-generated current in an ideal solar cell. It depends on the number of electron-hole pairs generated by the light flux incident on the front surface of the cell.
- **Open circuit voltage** V_{oc} corresponds to the zero current through the cell. It is defined by the steepness of the I-V curve of the p-n junction and depends on the minority charge carriers' recombination rate in the material of the cell.
- **Fill factor.** Although I_{sc} and V_{oc} are essentially the maximum current and the maximum voltage that can be withdrawn from the cell, the real situation (cell works as a power source for useful load) corresponds to some intermediate point on the I-V curve. The maximum output power point gives values of maximum current and voltage I_m and V_m. The fill factor is defined as:

$$\mathbf{FF = \frac{V_m * I_m}{V_{OC} * I_{SC}}} \qquad \textbf{Equation I.2}$$

  It is expressed in percent and depends generally on the resistive losses in the cell
- **Power conversion efficiency η** is defined as the ratio between maximum power output from the cell and power of the incident light:

$$\mathbf{\eta = \frac{P_m}{P_{in}} = \frac{V_m I_m}{P_{in}}} \qquad \textbf{Equation I.3}$$

2 Bulk recombination

Recombination mechanisms play a crucial role in the determination of the cell efficiency.

After the excess electron-hole pair has been created by photon absorption, the system tends to return to its equilibrium condition through a process called recombination: electron "falls" from the conduction band back to the valence band, thereby eliminating a valence-band hole. There are several recombination mechanisms important to the operation of solar cells – recombination through traps (defects) in the forbidden gap commonly referred to as Shockley–Read–Hall recombination, radiative (band-to-band) recombination, and Auger recombination.

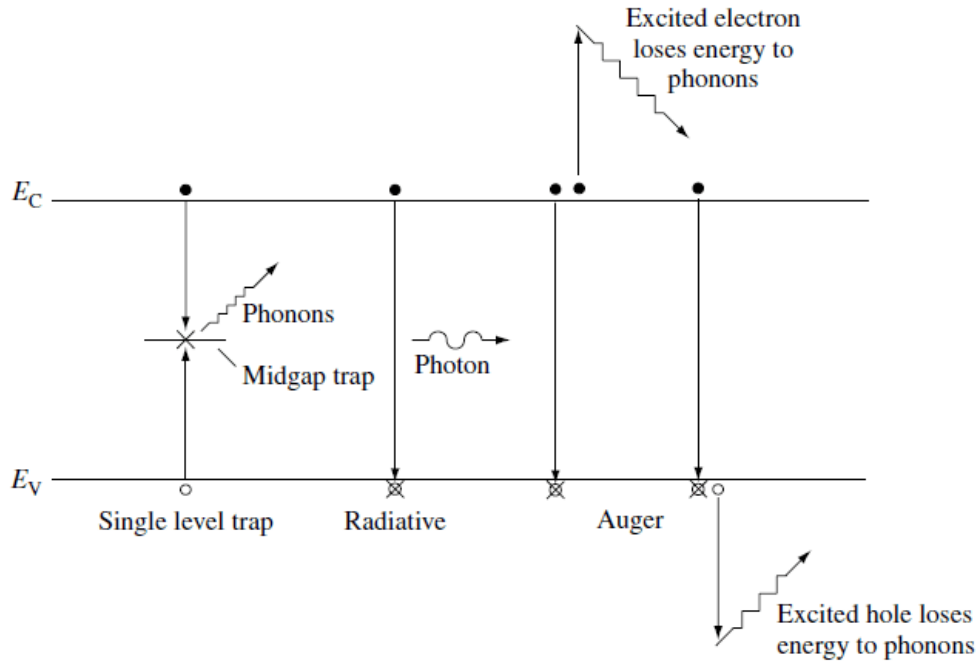

Figure 2 *Three different mechanisms of recombination in semiconductor.*

- *Radiative recombination*: an electron from the conduction band recombines with a hole from the valence band, emitting a photon. In Si, this type of recombination isn't significant due to the indirect band gap, hence, it will not be taken into account in the simulations.
- *Auger recombination:* an electron recombines with a hole, giving extra energy to another electron from the conduction band that in turn relaxes this energy as phonons. Auger recombination requires high enough carrier densities (10^{17} cm^{-3} at least).
- *Shockley-Reed-Hall (SRH):* recombination through the trap levels that impurities or crystal defects introduce into the forbidden gap of the host material. Defects, which can be centres of recombination, exist in the bulk of the cell material as well as on the front and rear surfaces.

For each recombination process, a net recombination rate per unit of volume U ($cm^{-3}.s^{-1}$) is defined as:

$$\mathbf{U} = \frac{\mathbf{\Delta n}}{\boldsymbol{\tau}} \qquad \textbf{Equation I.4}$$

where τ is the recombination lifetime that characterises the recombination process; and $\Delta n = n - n_0$ is the excess minority carrier density within the bulk (n_0 is the minority carrier density under thermo-dynamical equilibrium). From now on, Δn can refer to both electron and holes excess carrier densities, since we assume that both are equals. Indeed, electrons and holes are generated and recombine by pairs.

The total recombination rate in the bulk is then:

$$\mathbf{U_{Bulk} = U_{Rad} + U_{Aug} + U_{SRH} = \frac{\Delta n}{\tau_{Rad}} + \frac{\Delta n}{\tau_{Aug}} + \frac{\Delta n}{\tau_{SRH}}} \qquad \textbf{Equation I.5}$$

We can also define the bulk lifetime as:

$$\mathbf{\frac{1}{\tau_{Bulk}} = \frac{1}{\tau_{Rad}} + \frac{1}{\tau_{Aug}} + \frac{1}{\tau_{SRH}}} \qquad \textbf{Equation I.6}$$

Then:

$$\mathbf{U_{Bulk} = \frac{\Delta n}{\tau_{Bulk}}} \qquad \textbf{Equation I.7}$$

Excess carrier lifetime is one of the most important parameters affecting performance of solar cell.

3 Surface recombination and passivation

In the case of IBC solar cell, recombination at the surface is a crucial parameter for the cell efficiency.

At a semiconductor surface, the crystalline network is full of defects. For example, atoms at the surface have non-saturated bonds. Moreover, additional defects can be created during the fabrication process. Thus, a high velocity recombination process occurs at the surface. As for volume recombination, a net recombination rate per area U_S ($cm^{-2}.s^{-1}$) can be defined as:

$$\mathbf{U_s = S * \Delta n_s} \qquad \textbf{Equation I.8}$$

where Δn_s is the excess minority carrier density at the surface (cm^{-3}); and S is the surface recombination velocity. Due to the dimension of U_S ($cm^{-2}.s^{-1}$), S is usually measured in $cm.s^{-1}$ instead of a lifetime.

As recombination at the surface are mainly due to defects, the Shockley Read Hall model is used to describe this process [22]:

$$U_S = \frac{n_s p_s - n_i^2}{\frac{n_s + n_1}{S_p} + \frac{p_s + p_1}{S_n}}$$ **Equation I.9**

Where n_s and p_s are respectively the electrons and holes surface concentrations, S_n and S_p theirs respective surface recombination velocity and n_1 and p_1 are constants depending of traps' energy.

Looking at the model, we can identify two ways of decreasing the recombination process:

- First, we can decrease the surface recombination velocities; S_p and S_p. It is possible to do this by depositing a passivation layer with a low defects concentration at the Si interface. Reducing the number of defects at the interface reduces the surface recombination velocities. It is called a *chemical passivation.*

- The second way is to reduce the concentration of minority carriers. By depositing a passivation layer with a high concentration of trapped fixed charges, an electric field is created at the interface, reducing the concentration of minority charge carriers. It is called a *field passivation*.

A good passivation of p-doped and n-doped silicon can be achieved with an Al2O3 passivation layer [22]. The impressive performance of aluminium oxide layers is related to the combination of excellent chemical surface passivation, lowering the interface defect density, and oxide-trapped negative charges located near the semiconductor-oxide interface.[23]

Whereas the chemical passivation acts the same way on both p- and n-type silicon, the effect of the field passivation is a more delicate issue since the minority carriers are of opposite charge in p- and n-type. Figure 1.4 shows simulation results of the effect of Al_2O_3 passivation layer on both p- and n-type Si [23].

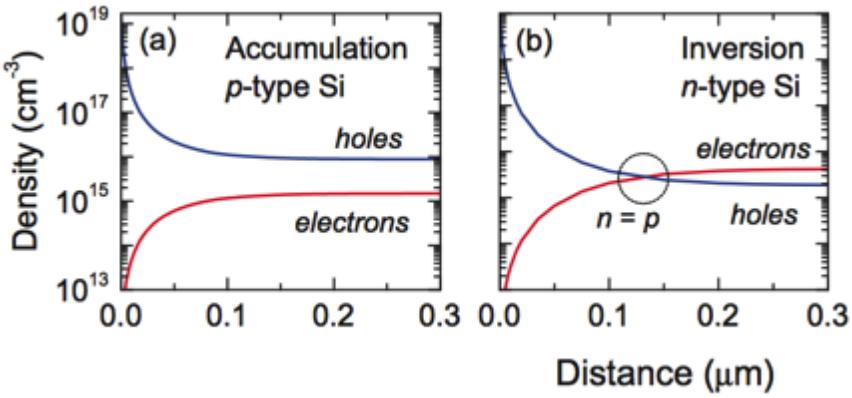

Figure I.1. *Electron and hole density below the Si surface for (a) p-type and (b) n-type Si under influence of a negative fixed surface charge of Q_f = -2*10^{12} cm^{-2}; Data simulated by PC1D for 2 Ohm/cm wafers under illumination [23].*

Al_2O_3 oxide charges usually exhibits negative polarity. Thus, the field effect is particularly efficient on p-type. On n-type, depending of the doping concentration, we can observe an inversion in carrier concentrations. At the near surface, the low electron concentration reduces the surface recombination the same way as for p-type.

II. Interdigitated-back-contact solar cells

1 Structure

Using a solar concentrator system in conjunction with solar cells reduce the solar cell area required per peak watt of output [5]. However, in order to benefit from the use of these concentrators the cells must be of high efficiency.

Schwartz and Lammert introduced the concept of "Interdigitated Back Contact" (IBC) solar cell (SC) in 1975. It was originally designed to overcome limitations of conventional designs for concentrating photovoltaic (CPV) applications. Over time, the IBC became the best silicon solar cell design for CPV applications and, to this date, is still the most efficient one, with efficiencies up to 27.6% in laboratory [1]. Later, the efficiency of one-sun IBC silicon solar cells increased from about 21% to 24.2% [6], making its design one of the most efficiency large-area solar cells designs for one-sun applications. A schematic drawing of the IBC design is shown in Figure II.1:

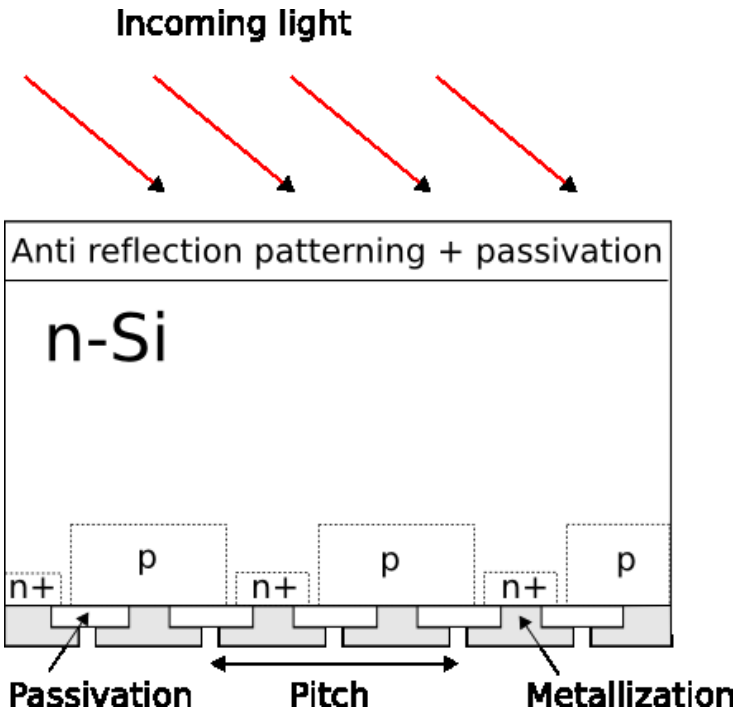

Figure II.1 *Interdigitated Back Contact Solar Cells*

The cell was originally designed with the emitter and back-surface field and the respective contacts forming an interdigitated finger pattern. The main particularity is that both the complete metallization and the complete contacted diffused region are located on the backside of the cell. In the last decades, new designs have been developed and the more general name "Back-Contact Back-Junction" (BC-BJ) has emerged.

2 Benefits

Having both the p-n junction and the complete metallization in the backside of the cell brings some major advantages over conventional solar cells designs.

In conventional solar cells, the front metallization reflect a large part of the incoming light. This phenomenon is called the "front-side shading" and is in the range of 6-9% [7]. A recent metallization technique lowered this range to 5-6% [7]. However, it still accounts for a significant reduction of solar cells' efficiency. On the contrary, no shading occurs in IBC solar cells due to absence of metallization on the front side. This leads to an increased short-circuit current (J_{SC}) of the cell and, thus, to an increased cell efficiency.

One of the great challenges in conventional solar cells design concerns the trade-off between low series resistance and high light absorbance. In IBC design, those two issues are solved separately on either side of the cell:

- On the *frontside*: due to absence of metallization, the surface can be optimized for light trapping and surface passivation properties.
- On the *backside*: Fingers widths are no longer limited by shading properties. The series resistance can be reduced which improve the fill factor and the cell efficiency.

Furthermore, as all electrical connections are in the same plane, the interconnection becomes potentially easier, cheaper and can be fully automated in the module assembly process, and the solar cell packaging density can be increased. State-of-the-art multi-crystalline cells with 16.5% cell efficiency will generally lead to a total area module efficiency of only 14% [8]. However, using IBC design, a module of 20.66% efficiency with 21.9% cell efficiency has been reported [1].

Finally, this design brings freedom in the choice of emitter profile. As a consequence, the problem of recombination in diffused region becomes less important, since the diffused regions are located far from the region of maximum photo-generation (c.f. Figure II.2).

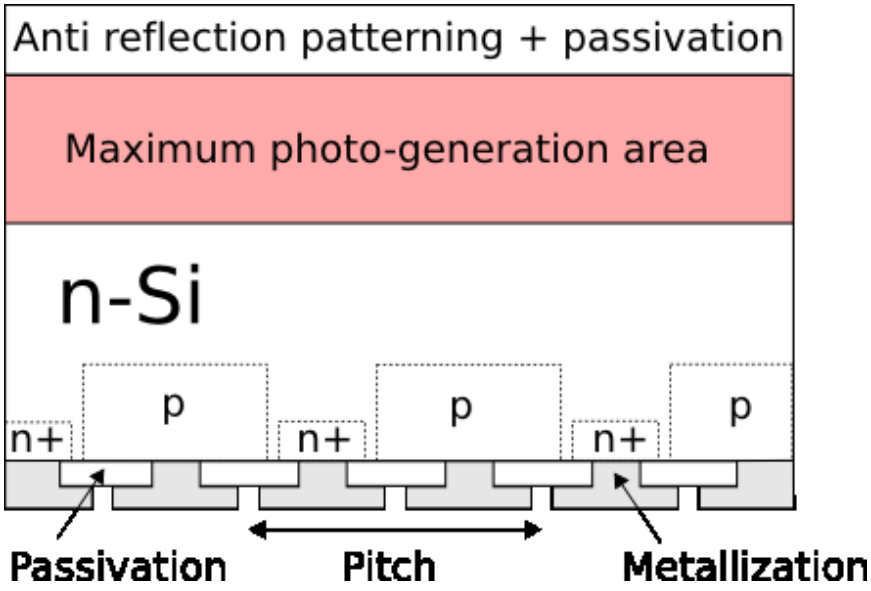

Figure II.2 *Maximum photo-generation area in an IBC solar cell*

3 Drawbacks

Although IBC design brings significant advantages, new challenges arise from this technology.

In solar cells, most of electron-hole pairs are generated near the front side. As the p-n junction is located at the rear side, minority carriers have to diffuse over a long distance to be collected. Thus, the probability of recombination in the base significantly increases. An increase of recombination losses in the base leads to lower Voc and decreases the energy conversion efficiency. Therefore, IBC solar cells usually require a higher semiconductor quality than conventional designs.

Reducing the thickness of the cell limits the recombination losses in the bulk, since the distance to the contact becomes shorter. However, a too thin cell would results in reduced light absorption in the semiconductor. A compromise between these two opposite effects can be achieved to find an optimum cell thickness at which the efficiency peaks. This optimum value is dependent on the bulk recombination rate.

In addition, excess carriers have to travel laterally to be collected. The longer is the pitch (c.f. Figure II.2) of the cell, the longer is the travelling distance. As for the previous effect, the probability of recombination in the base increases with the travelling distance, reducing the cell efficiency [9]. Figure II.3 illustrates this phenomenon. Reducing the pitch of the cell necessitate a high-resolution process, generally complex and expensive.

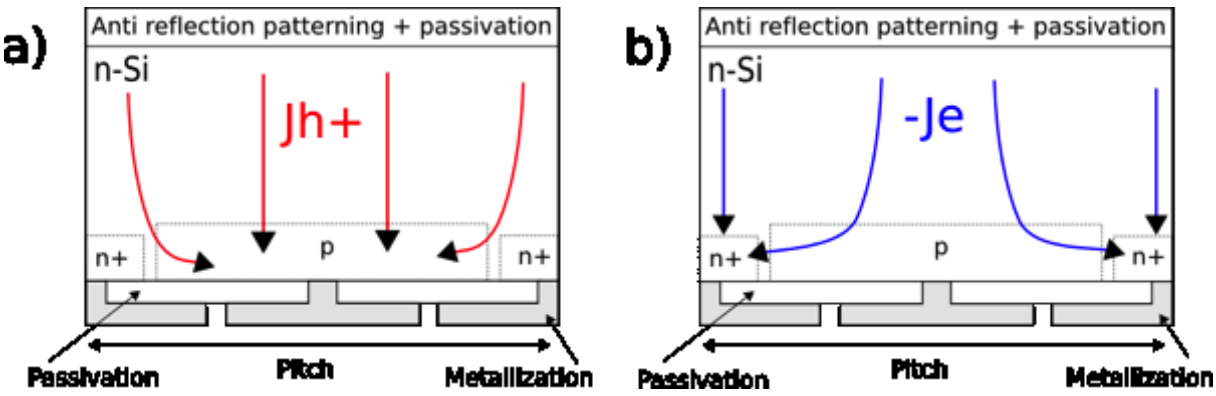

Figure II.3 *Lateral travelling of a) minority charges, b) majority charges.*

Moreover, some complications in the processing procedure come up from this design.

The processing of the backside requires 4 to 6 lithographic steps or at least one step in the simplified design [10]. This makes the processing procedure more challenging, complicated and thus more expensive than for conventional solar cells.

Moreover, there is a high risk of shunting between the p- and the n- electrode on the backside. Therefore, the masking process has to be very accurate in position and resolution, which results in increased complexity of the process and of the cost of the cell.

Some low-cost processes, without lithography, have been introduced in the last decade. However, those processes lead to a reduction of the resolution. This results in a pn pitch in the millimetre range, whereas the typical value is 45µm for a lithography process [9]. With a large pitch, majority carriers have to travel a long lateral distance and it results a diminution of the overall efficiency, as previously explained.

4 Requirements

It has been shown [11] that the front surface recombination velocity and the minority carrier lifetime in the bulk are critical parameters for the efficiency of a solar cell. The importance of both properties is illustrated in Figure II.4:

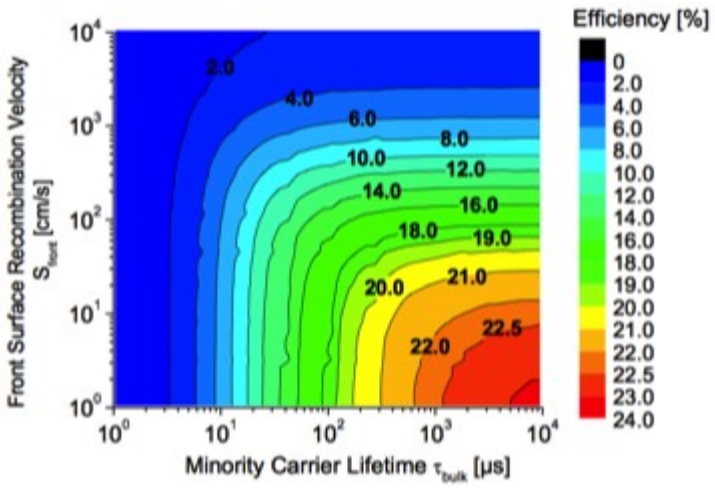

Figure II.4 *Simulations of the efficiency of a one-dimensional back-junction solar cell structure in a wide range of carrier lifetimes and front surface recombination velocity. The thickness of the simulated device is 200 µm. The resistivity of the n-type base is 1 Ω cm and the p-type rear emitter has a sheet resistance of 30 Ω/sq. Simulations were performed using PC1D[11].*

To achieve a high efficiency cell, the minority carrier lifetime in the bulk has to be as high as possible and, simultaneously, the front surface recombination velocity has to be as low as possible. When only one of those parameters is optimized, the other limits the efficiency of the cell. For instance, with a lifetime of 0.5ms in the bulk, the efficiency is almost constant with a front surface recombination velocity from 20cm.s^{-1} to 0 cm.s^{-1}.

The minority carrier diffusion length must be at least four times longer than the cell thickness of the cell [11]. This value can only be obtained by using a high quality substrate. For this reason, materials such as float-zone (FZ) or Czochralski (CZ) substrates with bulk carrier lifetime greater than 5 ms are generally preferred. For one-sun applications, the thickness of the cell is usually between 150 and 200 µm [12].

Simultaneously, the front-surface recombination velocity has to be kept as low as possible. Ideally, it should be much smaller than the ratio between the minority-carrier diffusion constant and the thickness of the cell [12], which is typically less than 10 cm/sec.

To achieve a SC with efficiency up to 22%, a substrate lifetime above 1000 µs and a surface recombination velocity below 10 cm/s are needed (Figure II.4). The passivation of the front surface becomes a critical feature in IBC-SC.

Moreover, it has been proven that n-type silicon substrates are more suitable for this application due to its larger tolerance to most common impurities compared to p-type Si. Moreover, n-type Czochralski (CZ) Si is free of light-induced degradation caused by boron–oxygen complexes.

5 Point-contact

In the last years, several variants in IBC design have been developed in order to increase the energy conversion efficiency. The Point Contact (PC) design is very similar to the IBC design in that sense that it has both electrical contacts on the backside. However, in the point-contact-cell, rather than having alternating n and p fingers, the contact metal is in contact with the silicon only in an array of points on the back surface. Figure II.5 illustrated this design.

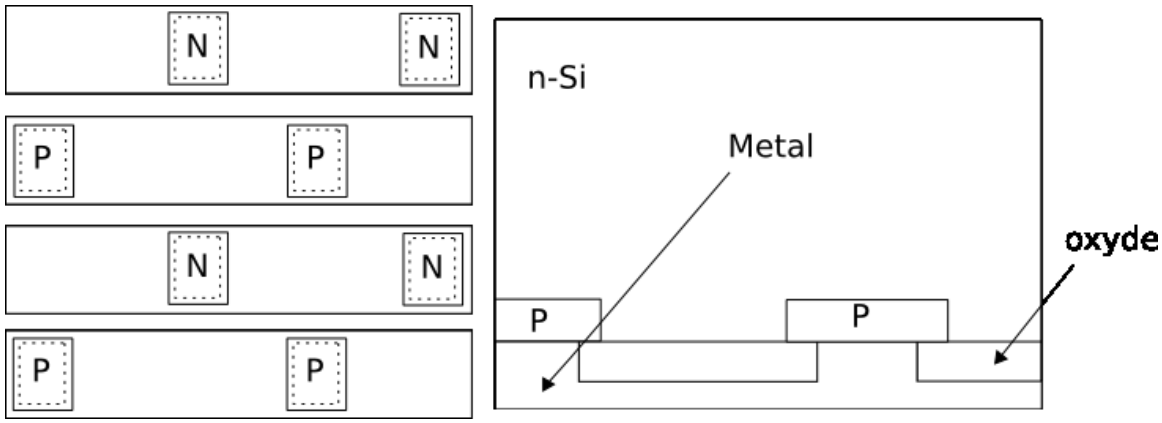

Figure II.5 *Structure of an IBC PC Solar cell.*

Conventional IBC solar cells are affected by significant recombination losses at the back metal-contacted interfaces. [13]. The main advantage of the point contact structure is to reduce the back-surface recombination velocity by reducing the contact coverage fraction.

Moreover, the effective internal bottom reflectivity is increased due to the larger reflectivity of c-Si/dielectric/metal stack interface (above 0.90) with respect to the metal/c-Si one (0.65) [13].

Originally developed for CPV applications (mostly due to the high processing cost), the point contact structure detains the record with an efficiency of 28.3% at 100 suns measured in laboratory [14]. At this date, it also detains the record of efficiency for large

area cells (155,1 cm^2) at one sun, with an efficiency of 24.2% reached by the third generation of SunPower solar cells [15].

III. Black-silicon

Black silicon (b-Si) is one kind of surface-nanostructured silicon with extremely low reflectivity. Reflectance values before 1 % in visible rang have been obtained [3]. It has been a subject of great interest in various fields, including photovoltaics. Indeed, its low reflectivity can potentially enhance the efficiency of solar cells to a new level. The first application of b-Si was the optimization of etching parameter in vertical wall etching using a reactive ion etching process (RIE) but later on it became an interesting solar cell surface texture.

1 Fabrication methods

Fabrication of three-dimensional structures necessitates high-selectivity etching processes. Some chemical wet etchings (KOH) provide good selectivity on c-Si, however those processes are constrained by crystal planes. Therefore, dry technology is indispensable for fabricating three-dimensional building blocks for MEMS applications. This has the advantage that not only single-crystalline silicon but also poly-crystalline and amorphous silicon can be used for the fabrication of three-dimensional structures. Moreover, it can be utilized to etch arbitrary shaped masks [16]. Dry etching has been achieved with several gas mixtures. SF6/O2 mixture produces anisotropic etching and has the advantage of being fluorine-based that can be used in common reaction ion etching systems [16].

1.1 Reactive ion etching process

SiF6/02 plasma provides a good anisotropic etching of Si. The principle of the etching is shown in Figure III.1.

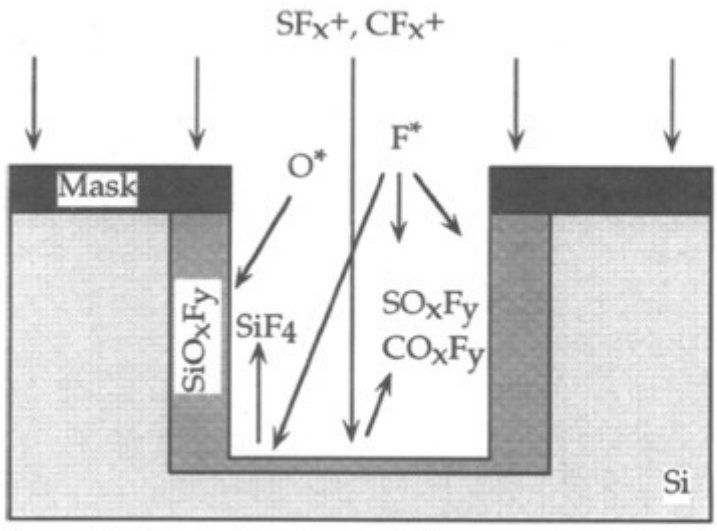

Figure III.1 *Schematic diagram of the etch mechanism of SF6/02gas system [17] .*

The anisotropic etching is explained by three mechanisms [17].

- SF6 produces the F* radicals for the chemical etching of Si, resulting in the formation of volatile SiF4;
- Oxygen produces the O* radicals to passivate the silicon surfaces with SixOyFz;
- SF6 is the source of SFx+ ions responsible for the one direction removal of the SixOyFz layer at the bottom of the etching trenches, which forms volatile SiOxFy.

In other words, the etching is a constant competition between the etching of fluorine radicals and the passivation of oxygen radicals. The etching is increased directionally thanks to the SFx+ ions [17]. Adjusting the different parameters results in different shapes as positive (Figure III.2 a) or negative (Figure III.2 b) tapered profiles.

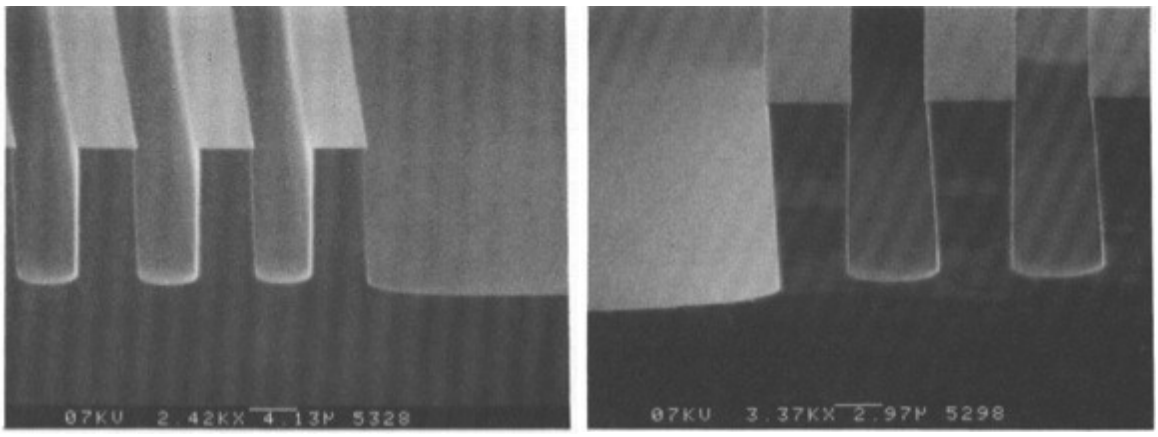

Figure III.2 (a) *Positive tapered profile [17]* (b) *Negative tapered profile [17]*

1.2 Black-silicon method

As stated in the above there is a constant competition between the fluorine radicals and the oxygen radicals. At a certain ratio, there is such a balance between the etching and the passivation that a nearly vertical wall results [18]. At the same moment native oxide, dust, and potentially other particles present in the reaction chamber will act as micro masks and, because of the directional etching, spikes will appear (Figure III.3); these spikes are also called “grass”. If the length of the spikes exceeds the wavelength of incoming light, this light will be “caught” in the area between the spikes and the silicon will appear black [18].

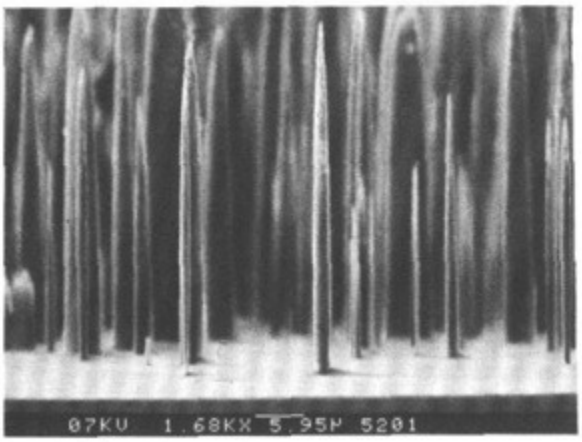

Figure III.3 *The formation of grass [18]*

Depending of the degree of anisotropy, different black-silicon profiles can be etched. The most anisotropic process results in needle-like shapes and the more isotropic it gets, the more pyramid-like shapes result [19]. Saleem H. Zaidi et al. investigated the RIE textured surface and the relative reflectivity depending on RIE parameters [20]. Figure III.4 shows the different profiles obtained.

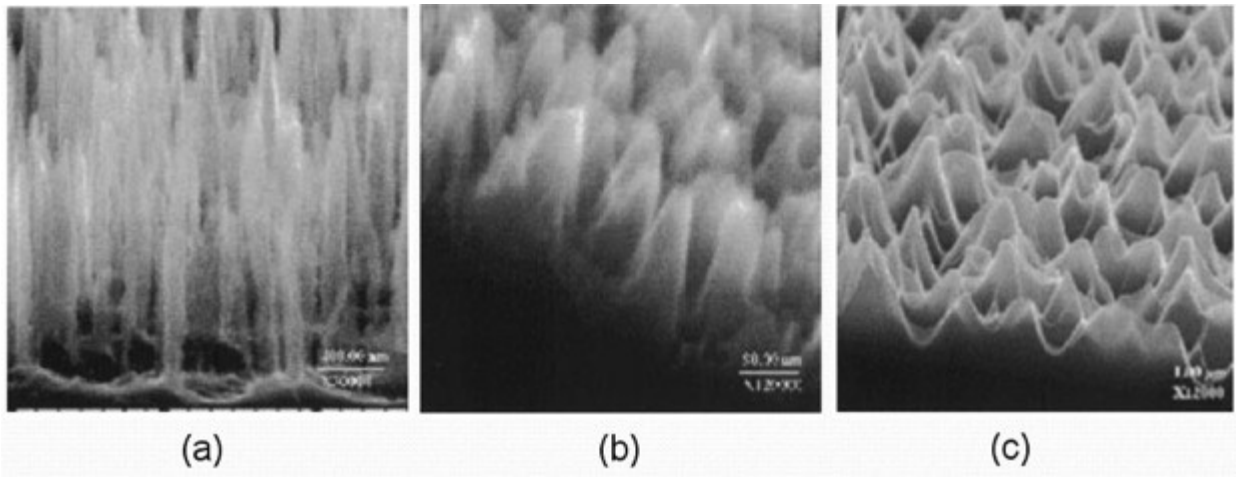

Figure III.4 *SEM pictures of different types of Si-textured profiles formed by RIE process variation: (a) needles (0.03 to 0.07 μm), (b) small pyramids (0.02 to 0.05 μm), and (c) large pyramids (0.1 to 0.6 μm) [20].*

The reflectivity of the surface is highly depending on the profile. Figure III.5 shows the reflectance measurements from the three textured profiles shown in Figure III.4. The lowest spectral reflection is from the small pyramids, and the large pyramids show higher UV and lower IR reflectance in comparison to needle-like features.

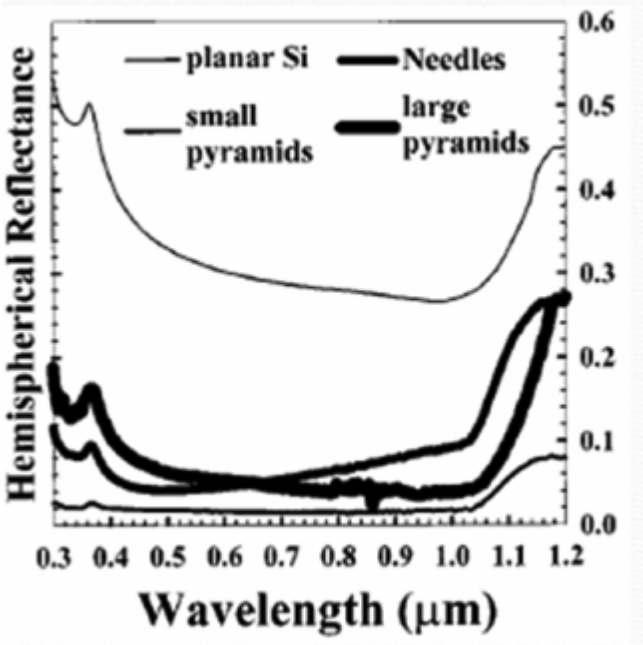

Figure III.5 *Hemispherical reflectance measurements from the three textured profiles shown in figure 10 [20].*

2 Benefits

In black-silicon, part the volume is air and the other part is silicon with the ratio varying from 100% air to 100% silicon. As the light propagates from the top surface into the sample, it passes through several layers with graduated refractive index. It results in significant advantages over randomly distributed pyramids, which is the most popular anti reflection technique used in silicon solar cells.

First of all, very low-reflectance over a brand rang of incidence wavelength can be obtained. A reflectance under 0.1 over wavelengths from 300nm to 1200nm has been measured with a needle profile (c.f. Figure III.5).

Moreover, contrary to others anti-reflecting techniques, black-silicon has a low reflectance over a large range of incident angles. Simulations predict a low reflectivity in the visible range for incidence angles up to 50° from the normal of the surface [21]. Figure III.6 draws those results.

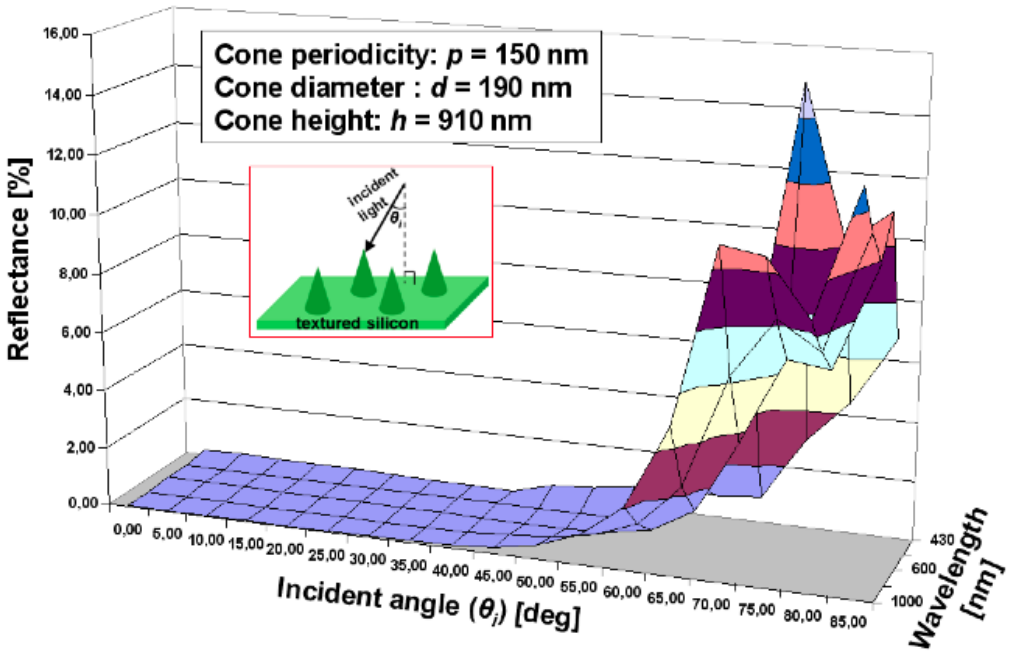

Figure III.6 *Example of simulated reflectivity with respect to the electric field incident angle.*

Another advantage of black-silicon texturing is that multi-crystalline silicon wafers can be very well textured using RIE [20]. Indeed, the randomly distributed pyramids technique is not effective in texturing of low-cost multi-crystalline wafers due to the varying crystallographic orientation.

Finally, the RIE process is low-cost, maskless and suitable for large-area cells [18, 20].

3 Drawbacks

However, some drawbacks make it not very suitable for solar-cells application [20]:

- A lot of defects are created at the surface during the process, resulting in significant surface recombination.
- The surface area is increased. Considering the surface recombination velocity and the excess carrier concentration constant on the surface, and integrating Equation I.8 over the surface results in a total number of surface recombination per second:

$$\mathbf{N_{R_s}} = \mathbf{S} * \Delta\mathbf{n_s} * \boldsymbol{A} \qquad \textbf{Equation III.1}$$

  where A is the surface area. Therefore, the increase of surface area also increases the number of surface recombination.
- The textured surface may not result in good ohmic contact due to non-compact contacts with electrodes.
- The structure of b-Si is not very strong and needles can be wiped off easily.

We can notice that the ohmic contact issue is irrelevant in the case of IBC solar cell since both metallization are in the backside (c.f. chapter 0.) Moreover, a lot of progresses have been done in the passivation of the black-silicon surface and nowadays very low surface recombination velocity can be achieved. Indeed, a recent study has demonstrated very low effective surface recombination velocity on black-silicon using Al_2O_3 passivation layer [3]. A lifetime around $\tau_{eff} = 1\,ms$, corresponding to effective surface recombination velocity of $S_{eff} = 22cm.s^{-1}$ has been measured on low-resistivity CZ wafer.

IV. Modeling effective surface recombination velocity

As illustrated in Figure II.4, the surface recombination velocity is a relevant parameter considering the cell efficiency. Hence, it is critical to perform a good passivation of the surface to obtain a high efficiency cell. The passivation is usually characterised by the effective surface recombination velocity, S_{eff}. The measurement of this parameter is explained in this chapter.

1 Model and approximations

We consider a silicon wafer with a bulk lifetime τ_{Bulk} and a front and rear surface recombination velocity, respectively, S_{Front} and S_{Rear}. Figure IV.1 illustrates the wafer. The surface of the wafer often contains fixed charges due to the passivation layer and an electric field is generated. Hence, we define for each surface a thin space charge region of width δ and we assume that:

- The *minority carrier concentration is constant (*Δn*)* outside of the space charge regions.
- There is *neither recombination nor photogeneration* in the space charge regions.

Those two approximations will be used afterward.

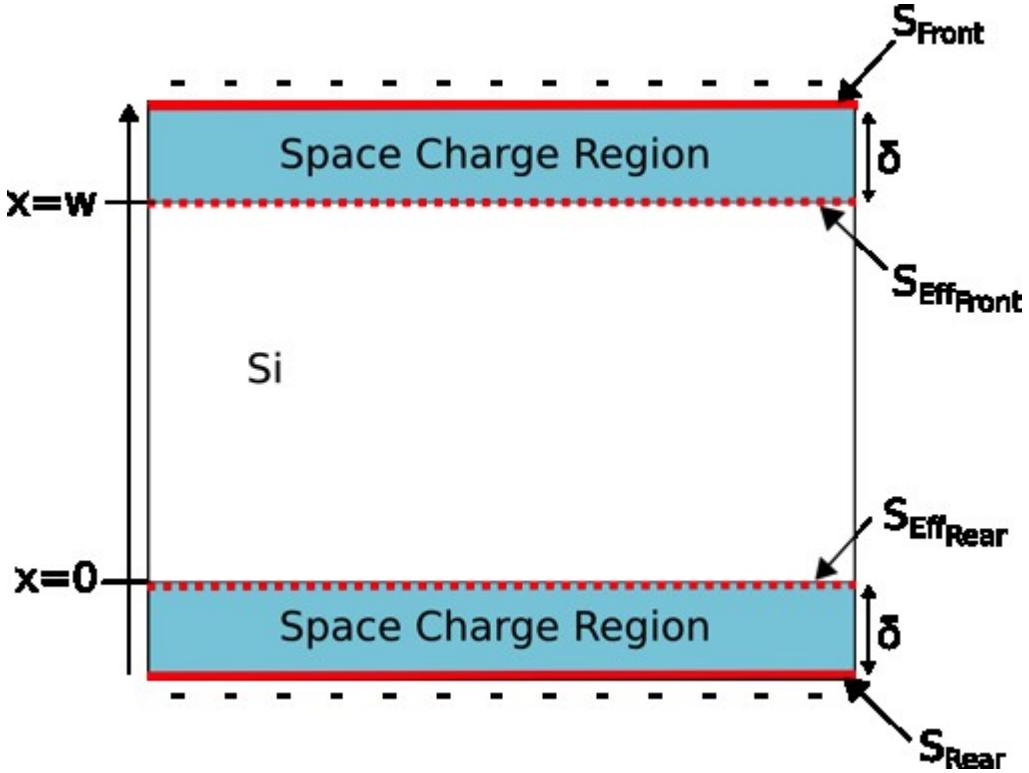

Figure IV.1 *Wafer with negative surface charge density and space charge region approximation.*

As the space charge regions are very thin, we can consider that the distance between the inner limits of the two space charge regions equals the total thickness of the cell. In other words:

$$\mathbf{w + 2\delta = w} \qquad \textbf{Equation IV.1}$$

2 Effective surface recombination velocity

Because of surface charges, Δn_s can be different from Δn. Hence, we define the effective recombination velocity S_{eff} (cm.s^{-1}) as follow:

$$\mathbf{U_s = S_{Eff} * \Delta n} \qquad \textbf{Equation IV.2}$$

where Δn (cm^{-3}) is the excess minority carrier density at the limit of the space charge region define at the surface. S_{eff} can be seen as the equivalent surface recombination velocity on an imaginary surface inside the wafer (c.f. Figure IV.1). We define the front and rear effective surface recombination velocity, respectively, $S_{Eff_{Front}}$ and $S_{Eff_{Rear}}$, accordingly to Equation IV.2.

3 Continuity equation inside the bulk

We start from the continuity equation for electron in the bulk:

$$\frac{\partial n(x,t)}{\partial t} = \frac{1}{q}\frac{\partial J_n(x,t)}{\partial x} - U(x,t) + G_L(x,t) \qquad \textbf{Equation IV.3}$$

where $J_n(x,t)$ is the current density of electrons in the bulk, $U(x,t)$ the total net recombination rate and $G_L(x,t)$ the photo-generation rate.

In steady-state conditions:

$$0 = \frac{1}{q}\frac{\partial J_n(x,t)}{\partial x} - U(x,t) + G_L(x,t) = \frac{1}{q}\frac{\partial J_n(x,t)}{\partial x} - \frac{\Delta n(x)}{\tau_b(\Delta n)} + G_L(x,t) \qquad \textbf{Equation IV.4}$$

By integration on the waver thickness:

$$0 = \frac{1}{q}\int_0^w \frac{dJ_n(x)}{dx}dx - \int_0^w \frac{\Delta n(x)}{\tau_b(\Delta n)}dx + \int_0^w G_L(x)dx \qquad \textbf{Equation IV.5}$$

Here, we assume that Δn is constant over the thickness of the cell. This approximation can be done since we consider the "reduced cell". Then, using the notation:

$$\langle \Delta n \rangle = \frac{1}{w} \int_o^w \Delta n(x)\, dx$$ **Equation IV.6**

we obtain:

$$0 \cong J_n(x=w) - J_n(x=0) - q \cdot w \cdot \frac{\langle \Delta n(x) \rangle}{\tau_b\left(\langle \Delta n \rangle\right)} + q \cdot w \cdot \langle G_L(x) \rangle$$ **Equation IV.7**

4 Current at the space charge region limit

Now, we need to evaluate $J_n(x = w)$ and $J_n(x = 0)$. We start from the continuity equation at the surface:

$$\frac{dn_s(t)}{dt} = \frac{J_n(x=-\delta,t)}{q} - U_s$$ **Equation IV.8**

Now, assume we can neglect recombination and photo-generation in the space charge region. Therefore, by continuity:

$$\frac{J_n(x=0,t)}{q} = \frac{J_n(x=-\delta,t)}{q}$$ **Equation IV.9**

Combining Equation IV.8 and Equation IV.9 we obtain:

$$\frac{dn_s(t)}{dt} = \frac{J_n(x=0,t)}{q} - U_s$$ **Equation IV.10**

Then at steady-state:

$$J_n(x=0,t) = qU_s$$ **Equation IV.11**

And by definition (Equation IV.2):

$$J_n(x=0,t) = qS_{EFF\_R}\Delta n(x=0)$$ **Equation IV.12**

The same way we deduce:

$$J_n(x=w,t) = -qS_{EFF\_F}\Delta n(x=w)$$ **Equation IV.13**

5 Effective lifetime

Introducing Equation IV.12 and Equation IV.13 in Equation IV.7 we obtain:

$$0 \cong -q(S_{EFF\_F}\Delta n(x=w) + S_{EFF\_R}\Delta n(x=0)) - q\cdot w\cdot \frac{\langle \Delta n(x)\rangle}{\tau_b(\langle \Delta n\rangle)} + q\cdot w\cdot \langle G_L(x)\rangle \qquad \textbf{Equation IV.14}$$

Keeping the approximation that Δn is constant:

$$0 \cong -\langle \Delta n(x)\rangle \left[\frac{(S_{EFF\_R} + S_{EFF\_F})}{w} + \frac{1}{\tau_b(\langle \Delta n\rangle)}\right] + \langle G_L(x)\rangle \qquad \textbf{Equation IV.15}$$

then we can define the effective lifetime as:

$$\frac{1}{\tau_{Eff}} \cong \left[\frac{(S_{EFF\_R} + S_{EFF\_F})}{w} + \frac{1}{\tau_b(\langle \Delta n\rangle)}\right] \qquad \textbf{Equation IV.16}$$

In the case of a symmetrical device:

$$\frac{1}{\tau_{Eff}} \cong \frac{2S_{EFF}}{w} + \frac{1}{\tau_b(\langle \Delta n\rangle)} \qquad \textbf{Equation IV.17}$$

And we obtain:

$$\frac{\langle \Delta n(x)\rangle}{\tau_{Eff}} = \langle G_L(x)\rangle \qquad \textbf{Equation IV.18}$$

From Equation IV.18, using a sensor that can be calibrated to measure average carrier density in the sample, a light-intensity sensor and a calculation or measurement of resulting photogeneration, we can measure τ_{eff} in quasi-steady-state (QSS) or steady-state [24]. The average carrier density can be extracted from the excess conductivity using the following formula [25]:

$$\Delta\sigma = q(\mu_n + \mu_p)\cdot \Delta n \qquad \textbf{Equation IV.19}$$

Where $\Delta\sigma$ is the excess conductivity and μ_n and μ_p are respectively the electron and hole mobility. By integration over the thickness of the cell, and assuming that μ_n and μ_p are constants:

$$\langle \Delta\sigma(t) \rangle = q(\mu_n + \mu_p) \cdot \langle \Delta n(t) \rangle$$ **Equation IV.20**

Where:

$$\langle \Delta\sigma(t) \rangle = \frac{1}{w} \int_{x=0}^{w} \Delta\sigma(t,x)dx$$ **Equation IV.21**

Introducing Equation IV.20 in Equation IV.18 we obtain:

$$\tau_{eff} = \frac{\langle \Delta\sigma(t) \rangle}{q(\mu_n + \mu_p)\langle G_L(x) \rangle}$$ **Equation IV.22**

6 Bulk lifetime

In the previous chapter we derived the equation of τ_{eff}. In case of high quality wafers, it is common to neglect the bulk recombination and approximate:

$$\frac{1}{\tau_{eff}} = 2 * \frac{S_{eff}}{w}$$ **Equation IV.23**

However, this approximation is no longer valid in case of very good surface passivation. Hence, it is necessary to evaluate bulk lifetime and extract it from the effective lifetime. Using the following equation:

$$S_{eff} = \frac{w}{2} * (\frac{1}{\tau_{eff}} - \frac{1}{\tau_{bulk}})$$ **Equation IV.24**

The bulk lifetime depends of three recombination mechanisms: Shockley-Read-Hall, band to band and Auger recombination. It results in the following equation:

$$\frac{1}{\tau_{bulk}} = \frac{1}{\tau_{SRH}} + \frac{1}{\tau_{Rad}} + \frac{1}{\tau_{Aug}} = \frac{U_{Rad} + U_{Aug} + R_{SRH}}{\Delta n}$$ **Equation IV.25**

U_{rad}, U_{Aug} and R_{SRH} are the recombination rates ($cm^{-3}.s^{-1}$), Δn is the injection level (cm^{-3}) and $\tau_{SRH}, \tau_{Rad}, \tau_{Aug}$ are the lifetimes associated with each recombination mechanism (s). Auger and radiative recombination can be modelled with following equations [26]:

$$U_{Aug} = (p * n - n_i^2) * (C_n * n + C_p * p)$$ **Equation IV.26**

$$U_{Rad} = (p * n - n_i^2) * B$$ **Equation IV.27**

where B is the band to band recombination parameter,

$$C_n = C_{n_{LLI}} * \left(\frac{N_D}{N_D + p}\right) + \frac{C_{HLI}}{2} * \left(\frac{p}{N_D + p}\right) \quad \textbf{Equation IV.28}$$

and,

$$C_p = C_{p_{LLI}} * \left(\frac{N_A}{N_A + n}\right) + \frac{C_{HLI}}{2} * \left(\frac{n}{N_A + n}\right) \quad \textbf{Equation IV.29}$$

where $C_{n_{LLI}}$, $C_{p_{LLI}}$ and C_{HLI} are parameters depending of the material.

Shockley-Read-Hall recombination can be modelled with the following equation [27]:

$$R_{SRH} = \frac{np - n_i^2}{\tau_{p0}\left(n + N_c \exp\left(\frac{E_t - E_c}{kT}\right)\right) + \tau_{n0}(p + N_V \exp\left(\frac{E_V - E_t}{kT}\right))} \quad \textbf{Equation IV.30}$$

Where τ_{p0}, τ_{n0} are parameters depending of the material and E_t is the ernegy of traps. Usually, we use $E_t = 0$ as it is the most efficient trap energy.

7 Comparison of model to experiments

In our experiments, the front surface of the solar cell is passivated with Al_2O_3 layer grown by Atomic Layer Deposition. In order to know the surface recombination velocity of the front surface, we performed lifetime measurement on symmetrical wafers.

Magnetic Czochralski (Mcz) <100> n-type wafers with a bulk resistivity of ~2.2 Ohms and a thickness of 400µm were used as a substrate. Black-silicon has been grown on both side of the wafer by RIE. The wafers received a Radio Corporation of America (RCA) clean followed by a DI-wafer rinse prior to the deposition of Al_2O_3 films. The Al_2O_3 films were grown on both sides of the wafers by Atomic Layer Deposition (ALD) using trimethylaluminum and water. Deposition was done at a substrate temperature of 200°C. The number of cycles was chosen so that a 20nm film was obtained. After the deposition, the samples received a post-deposition anneal in N_2 at 400°C for 10 minutes.

7.1 Simulated bulk lifetime

In purpose of calculating the bulk lifetime, we simulate the device presented in Figure IV.1 with the simulation software PC1D. The simulation is performed with the following parameters.

$C_{n_{LLI}}$	$C_{p_{LLI}}$	C_{HLI}	B
$2.8 \times 10^{-31} cm^6.s^{-1}$	$9.9 \times 10^{-32} cm^6.s^{-1}$	$1.66 \times 10^{-30} cm^6.s^{-1}$	$9.5 \times 10^{-15} cm^3.s^{-1}$

τ_{p0}	τ_{n0}	E_t
$7\ ms$	$7\ ms$	0

Table IV.1 Shockley-Read-Hall**,** *Auger, band-to-band parameters for Mcz silicon [26, 28]*

Also, surface recombination parameters are set to zero. Hence, from Equation IV.17 the bulk lifetime equals the effective lifetime. The effective lifetime is calculated using Equation IV.25. Every term in the right-hand of the equation are calculated by PC1D. The results of the calculation are plotted in Figure IV.2. For an excess carrier concentration of $\Delta n = 1 * 10^{15} cm^{-3}$ the intrinsic lifetime is $\tau_{bulk} = 6.6\ ms$.

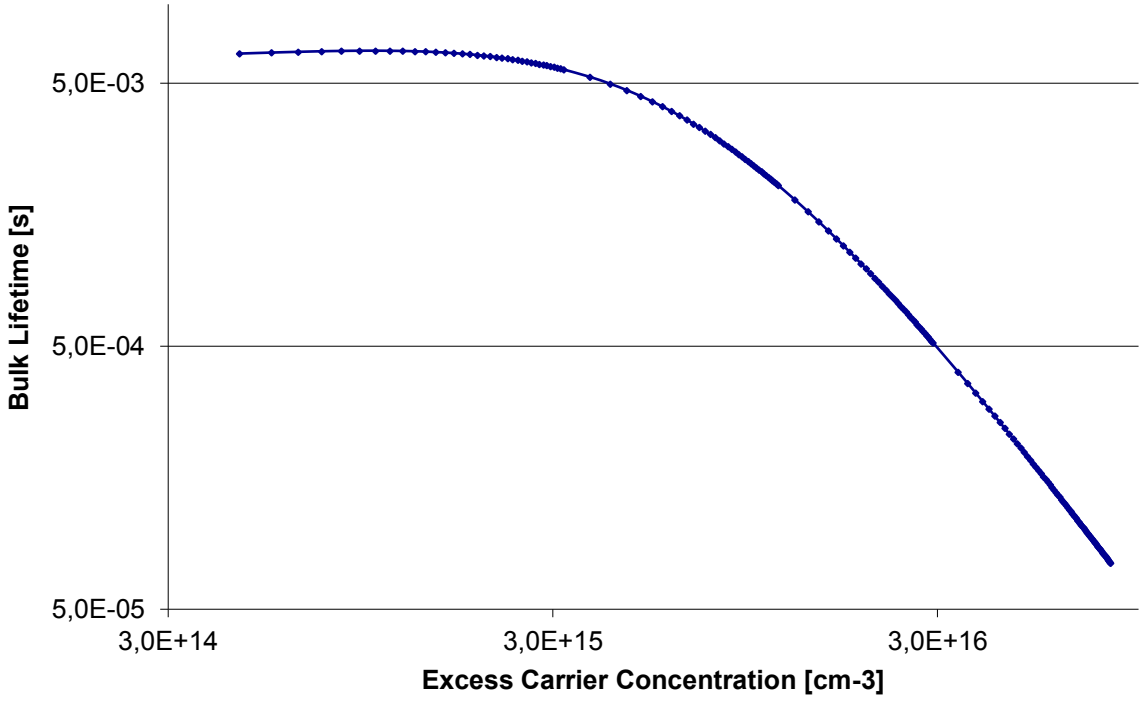

Figure IV.2 *Calculated bulk lifetime. Simulation with PC1D.*

7.2 Experimental lifetime

The effective minority lifetime of the samples was measured by contactless photoconductance decay (PCD) measurements in quasi-steady-state (QSS) [29] with Sinton Lifetime Tester (WCT-120). Figure IV.3 plots the results of lifetime measurement.

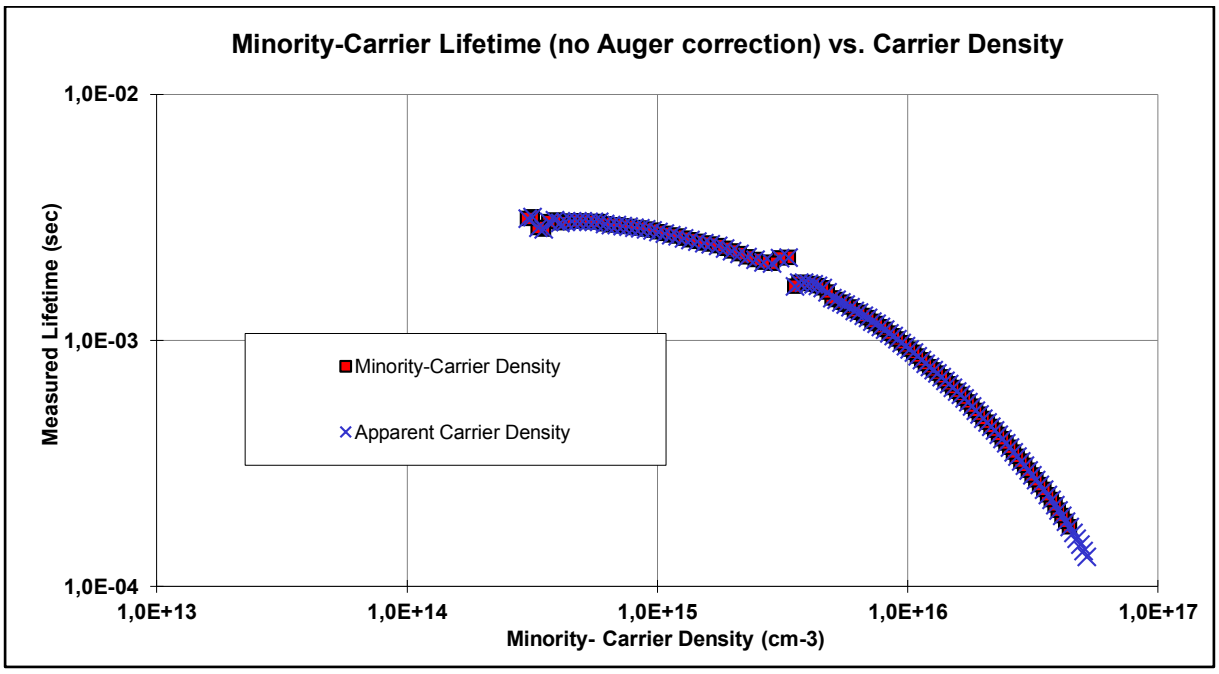

Figure IV.3 *Minority carrier lifetime measurement by PCD in QSS of n-type b-Si sample with Al_2O_3 passivation. The deposition and post-deposition parameters were similar to those used in the IBC cell processing.*

At a minority carrier density of $\Delta n = 1 * 10^{15} cm^{-3}$, the measured minority carrier effective lifetime is $\tau_{eff} = 2.78\ ms$. Then we can calculate S_{eff} from Equation IV.24 and we obtain: $S_{eff} = 4.16\ cm.s^{-1}$.

V. Development of the simulation model

1 ATLAS

Silvaco ATLAS is a physically based device simulator that enables to simulate the electrical, optical, and thermal behaviour of semiconductor devices physics in two or three dimensions. The idea of using physically based simulation is to gain data difficult or impossible to measure.

Silvaco ATLAS uses finite element analysis. In other words, the device in question is approximated onto a two or three-dimensional grid with a number of grid points called nodes. The transport of carriers through a structure can be modelled by applying to the node a set of differential equations derived from Maxwell's equations. These equations include Poisson's equation, the continuity equations and the transport equations. Poisson's equation combines the variations in electrostatic potential and the local charge densities. The electron and holes densities change as a result of generation, recombination, and transport processes that are taken into account by using the transport and continuity equations.

The equations are solved by an iterative method. The software chooses initials values and the next step state is calculated using the equations. If the values converge, the simulation stops when the change between two steps is less than a defined value. If the initial values are too far from the convergence, the simulation may diverge. In purpose of preventing divergence or making the convergence faster, it is possible to use intermediate steps. In this case, the illumination is simulated at intermediate values from zero to one sun.

Basic simulation steps are:

- Creation of the grid, i.e. the definition of the structure and regions and the node points.
- Determination of material parameters (doping, traps etc.) and models used.
- Solution in thermo-dynamical equilibrium.
- Calculation of I-V curve under illumination.

2 Physical models

ATLAS provides a variety of physical models that can be used in simulations. Table V.1 lists models used in this thesis.

Model	ATLAS Abbreviation
Fermi-Dirac	FERMI
Band-gap Narrowing	BGN
Carrier-Carrier Scattering	CCSMOB
Parallel Electric Field Dependence	FLDMOB
Shockley-Read-Hall	SRH
Concentration Dependence	CONSRH
Auger recombination	AUGER
Surface recombination	S.N S.P

Table V.1 *List of models used in the thesis*

Theses models are described in the following chapters.

2.1 Band-gap narrowing

Band Gap narrowing describes how heavy doping (greater then $10^{18}\,cm^{-3}$) alters the band gap by lowering the conduction band energy the same amount as raising the valence band. The expression used in Atlas is from Slotboom and de Graaf [30] :

$$\Delta E_g = BGN.E\left(\ln\left(\frac{N}{BGN.N}\right) + \sqrt{\ln\left(\frac{N}{BGN.N}\right)^2 + BGN.C}\right) \qquad \textbf{Equation V.1}$$

Where N is the doping concentration and BGN.E, BGN.N and BGN.C are parameters depending of the material. Defaults values by Slotboom and de Graaf are listed in Table V.2 [30].

Parameter	Default value
BGN.E (V)	$9.0\ 10^{-3}$
BGN.N (cm^{-3})	$1.0\ 10^{17}$
BGN.C	0.9

Table V.2 *The default values used for the simulation of band gap narrowing*

2.2 Carrier-carrier scattering

The carrier-carrier scattering model gives the low field electron and hole motilities (μn0 and μp0) function of the lattice temperature, the carriers concentrations and multiples parameters. The detail of the expression is given in the ATLAS user's manual in section 3.6.1.

2.3 Parallel electric field dependence

The parallel electric field-dependent mobility is modelled using the expressions:

$$\mu_n(F) = \mu_{n0}\left[\frac{1}{1+\left(\frac{\mu_{n0}F}{VSATN}\right)^{BETAN}}\right]^{\frac{1}{BETAN}} \qquad \textbf{Equation V.2}$$

$$\mu_p(F) = \mu_{p0}\left[\frac{1}{1+\left(\frac{\mu_{p0}F}{VSATN}\right)^{BETAN}}\right]^{\frac{1}{BETAN}} \qquad \textbf{Equation V.3}$$

where μ_{n0} and μ_{p0} are the low field electron and hole mobilities, F the electric field. VSATN and VSATP are saturation velocities for electron and holes that are user-definable. BETAN and BETAP are constants with default values of 2.0 and 1.0, respectively. By default, VSATN and VSATP are calculated from the temperature-dependent models:

$$VSATN = ALPHAN.\frac{FLD}{1+THETAN.FLDexp\left(\frac{T_L}{TNOM.FLD}\right)} \qquad \textbf{Equation V.4}$$

$$VSATP = FALPHAP.\frac{FLD}{1+THETAP.FLDexp\left(\frac{T_L}{TNOM.FLD}\right)} \qquad \textbf{Equation V.5}$$

Where ALPHAN.FLD, ALPHAP.FLD, THETAN.FLD, THETAP.FLD, TNOMN.FLD and TNOMP.FLD are user-definable parameters with defaults values listed in Table V.3.

Parameter	ALPHAN(P).FLD (cm/s)	THETAN(P).FLD	TNOMN(P).FLD (K)
Default value	$2.4x10^7$	0.8	600.0

Table V.3 *The default values used for the simulation of parallel electric field dependence*

2.4 Shockley-Read-Hall recombination

Shockley-Read-Hall recombination is modelled using the expression:

$$\mathbf{R_{SRH}} = \frac{\boldsymbol{pn - n_{ie}^2}}{\boldsymbol{TAUP0}\left[\boldsymbol{n + n_{ie}}\exp\left(\frac{\boldsymbol{ETRAP}}{\boldsymbol{kT_L}}\right)\right] + \boldsymbol{TAUN0}\left[\boldsymbol{p + n_{ie}}\exp\left(-\frac{\boldsymbol{ETRAP}}{\boldsymbol{kT_L}}\right)\right]} \qquad \textbf{Equation V.6}$$

Where T_L is the lattice temperature in Kelvin, ETRAP is the difference between the trap energy level and the intrinsic Fermi level and TAUN0 and TAUP0 are the electron and hole lifetime parameters. ETRAP is set to zero by default since the most efficient recombination centres are located in the middle of the bandgap.

2.5 Concentration dependence in Shockley-Read-Hall recombination

The constant carrier lifetimes that are used in the SRH recombination model above cans be made a function of impurity concentration using following equation:

$$\mathbf{R_{SRH}} = \frac{\boldsymbol{pn - n_{ie}^2}}{\boldsymbol{\tau_p}\left[\boldsymbol{n + n_{ie}}\exp\left(\frac{\boldsymbol{ETRAP}}{\boldsymbol{kT_L}}\right)\right] + \boldsymbol{\tau_n}\left[\boldsymbol{p + n_{ie}}\exp\left(-\frac{\boldsymbol{ETRAP}}{\boldsymbol{kT_L}}\right)\right]} \qquad \textbf{Equation V.7}$$

where:

$$\tau_n = \frac{TAUN0}{AN + BN\left(\frac{N_{Total}}{NSRHN}\right) + CN\left(\frac{N_{Total}}{NSRHN}\right)^{EN}} \qquad \textbf{Equation V.8}$$

$$\tau_p = \frac{TAUP0}{AP + BP\left(\frac{N_{Total}}{NSRHN}\right) + CP\left(\frac{N_{Total}}{NSRHN}\right)^{EN}} \qquad \textbf{Equation V.9}$$

Here, N is the local (total) impurity concentration. NSRHN and NSRHP parameters are user-defined. Defaults values are listed in Table V.4.

Parameter	TAUN0 (s)	TAUP0 (s)	NSRHN (cm^{-3})	NSRHP (cm^{-3})	AN,AP BN,BP	CN,CP EN,EP
Default value	1.0×10^{-7}	1.0×10^{-7}	5.0×10^{16}	5.0×10^{16}	1	0

Table V.4 *The default values used for the simulation of SRH recombination*

2.6 Auger recombination

Auger recombination is modelled using the expression:

$$R_{AUGER} = AUGN\ (pn^2 - nn_{ie}^2) + AUGP\ (np^2 - pn_{ie}^2) \qquad \textbf{Equation V.10}$$

Where n_{ie} is the effective intrinsic concentration and AUGN and AUGP are user-definable parameters depending of the material. Default values are listed in Table V.5.

Parameter	Default value
AUGN (cm^6/s)	$2.8x10^{-31}$
AUGP (cm^6/s)	$9.9x10^{-32}$

Table V.5 *The default values used for the simulation of Auger recombination*

2.7 Surface recombination

The recombination rate at the surface is modelled using the expression:

$$R_{surf} = \frac{pn - n_{ie}^2}{\tau_p^{eff}\left[n + n_{ie}\exp\left(\frac{ETRAP}{kT_L}\right)\right] + \tau_n^{eff}\left[p + n_{ie}\exp\left(-\frac{ETRAP}{kT_L}\right)\right]} \qquad \textbf{Equation V.11}$$

Here:

$$\frac{1}{\tau_n^{eff}} = \frac{1}{\tau_n^i} + \frac{d_i}{A_i} * S.N \qquad \textbf{Equation V.12}$$

And:

$$\frac{1}{\tau_p^{eff}} = \frac{1}{\tau_p^i} + \frac{d_i}{A_i} * S.P \qquad \textbf{Equation V.13}$$

$\tau^i_{n(p)}$ is the bulk lifetime calculated for node *i*. A_i and d_i are the area and the length for node *i*. The S.N and S.P parameters are the recombination velocity for electrons and holes respectively, which are user-definable. S.N and S.P default values are zero.

3 Simulation parameters

The structure of the simulated cell is depicted in this chapter. It corresponds to the structure of cells performed in the micro- and nano-technology laboratory of UPC Barcelona. Every parameter is chosen accordingly to the experiment.

3.1 Geometry

The cell is simulated in two dimensions. The structure of the cell is depicted in Figure V.1 (not scaled). For the purpose of increasing the speed of the simulations, only half of a pitch is simulated.

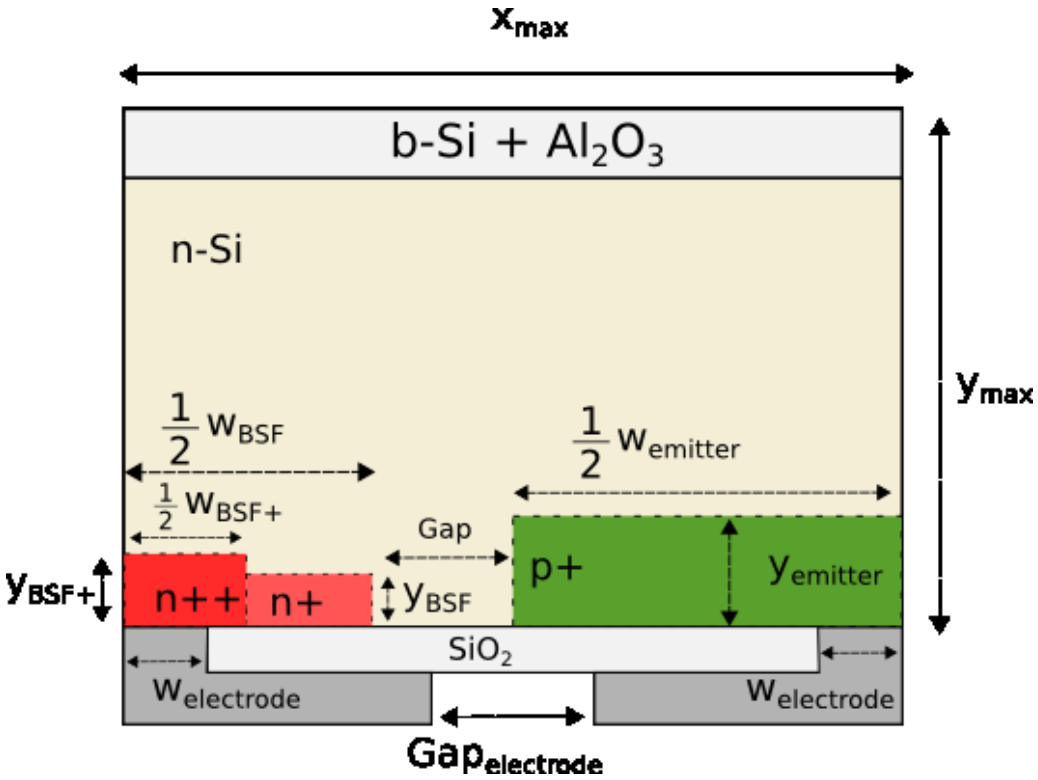

Figure V.1 *Structure of the simulated IBC solar cell.*

Default values used in this these are given in **Table V.6**.

Parameter	x_{max}	y_{max}	$w_{electrode}$	w_{BSF}	w_{BSF+}	**Gap**
Value	500 µm	220 µm	25µm	210µm	90µm	40µm

Parameter	$Gap_{electrode}$	y_{BSF+}	y_{BSF}	$y_{emitter}$	$w_{emitter}$
Value	80µm	2.3µm	1.1µm	5µm	710 µm

Table V.6 *Default values of simulation's parameters.*

3.2 Doping parameters

The cell is composed of four areas: the base, the emitter, the back surface field (BSF), and the high doping back surface field (BSF+). Doping parameters of each area are given in **Table V.7**.

Base		
Phosphorous density		$3.5 * 10^{15}\ cm^{-3}$
Resistivity	*bulkRes*	$1.4\ Ohm.cm$
BSF		
Peak of phosphorous density	BSFNpeak	$0.9 * 10^{19} cm^{-3}$
BSF+		
Peak of phosphorous density	BSFHighNPeak	$6 * 10^{19} cm^{-3}$
Emitter		
Peak of boron density	EmitterNPeak	$1 * 10^{19} cm^{-3}$

Table V.7 *Doping parameters of the reference cell*

3.3 Anti-reflection layer

Experiments were performed with two different anti-reflection methods: black-silicon and random pyramids. Both surface reflectances have been measured. For the purpose of simulating the surface, a weighted spectrum is calculated from the AM1.5G spectrum and reflectance data.

First, the AM1.5G spectrum is smoothed so that the spectral irradiance integral in each 5 nm wavelength interval is the same in both spectrums. This is done to match the wavelengths intervals of the reflectance measurements presented in the following subsection The spectrum in Figure V.2 was then used to calculate the effective spectrum in the cell by weighting by the reflectance of each anti-reflection method.

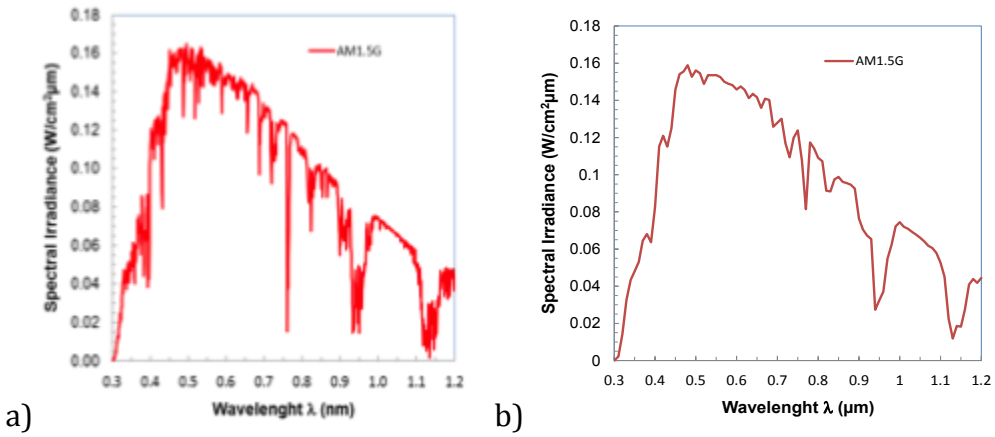

a) b)

Figure V.2. *Spectrum of (a) initial AM1.5G (b) smoothed AM1.5G.*

3.3.1 Black-silicon

Black-silicon presents a very low reflectance and a very good light trapping. Measurements of reflectance are presented in Figure V.3 (a). The smoothed AM1.5G of Figure V.3 was weighted with reflectance experimental results of b-Si and is presented in Figure V.3 (b).

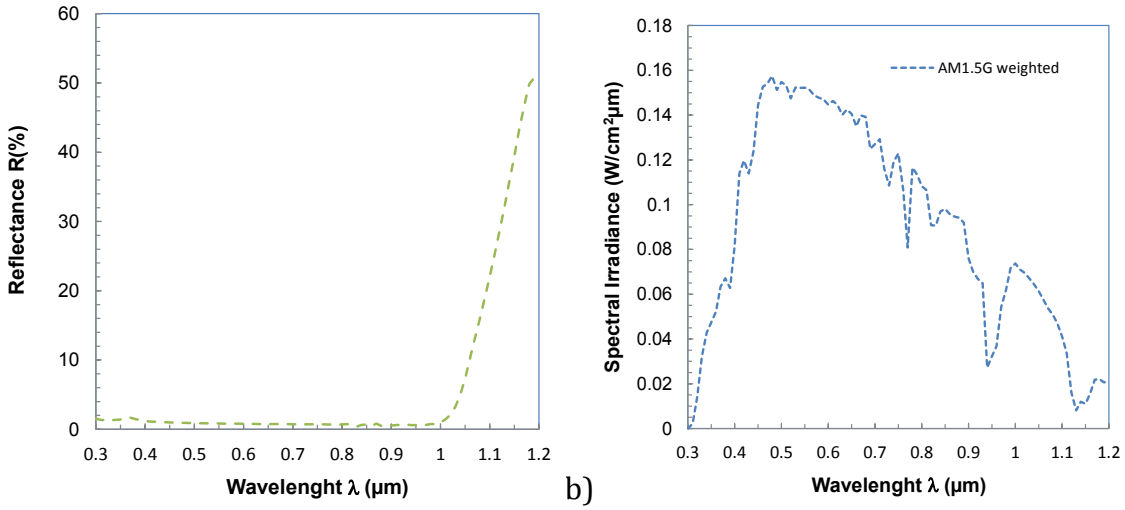

a) b)

Figure V.3 *(a) Reflectance experimental results of b-Si, (b) weighted AM1.5G spectrum*

This new spectrum is introduced directly into the cell at the top interface. Then, it is important to note that the reflectance measurement include the internal reflectance at the back of the cell. Hence, we have to take 100% internal reflectance on the front surface.

3.3.2 Random pyramids

The same method is used with random pyramids texturized surface. Figure V.4 presents the reflectance measurements (a) and the weighted spectrum (b).

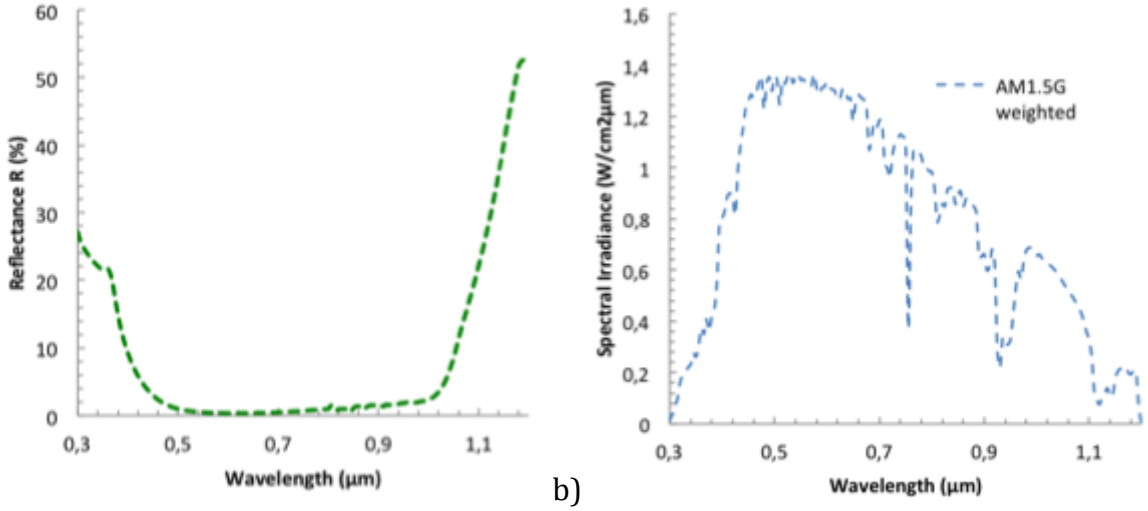

a) b)

Figure V.4 *(a) Reflectance experimental results of random pyramids, (b) weighted AM1.5G spectrum*

3.4 Front surface recombination velocity with surface charges

The front surface of the cell is passivated with aluminum oxide layer grown by atomic layer deposition. One characteristic of this passivation technique is that a high density of negative charges is trapped at the Si/Al_2O_3 interface during the growth. The fixed charge density typically varies from $Qf = -2 \times 10^{12} cm^{-2}$ to $Qf = -10 \times 10^{12} cm^{-2}$ [23, 31]. In the first place, we tried to simulate the cell with the following a surface charge density: $Qf = -5 * 10^{12}\ cm^{-2}$

The passivation was simulated via the parameters S.N. and S.P. (Equation V.11). The better the passivation, the lower those values are, and vice versa. Unfortunately, those values are not directly measurable. However, experimentally, we can easily measure the *effective minority carrier lifetime,* τ_{eff}, in function of the *average excess carrier density,* $\langle \Delta n \rangle$. This parameter is a good indicator of the surface passivation quality, but it depends of many phenomena. Hence, it cannot be used as a parameter in simulations. In order to use correct parameters in simulations, it is necessary to extract the parameters S.N and S.P from the measured τ_{eff}.

Using PC1D, we simulated the device presented in Figure IV.1. In this case, we assumed the device is symmetrical and therefore, $S_{Eff_{Front}} = S_{Eff_{Rear}} = S_{Eff}$. Moreover, we assumed that $S_n = S_p$.

PC1D calculates the excess conductivity due to the excess minority carrier density, as well as the photogeneration. Those outputs were used in Equation IV.22 to calculate τ_{eff}. S_n and S_p are input parameters. We used an input file to slowly increase the light and assuming a quasi-steady-state.

Simulations were performed with several values of S_n, S_p and with a surface charge concentration $QF = -5 * 10^{12}\ cm^{-2}$. Shockley-Read-Hall lifetimes are set accordingly to Mcz record bulk lifetime: $\tau_{p0} = \tau_{n0} = 7ms$ [28]. For each (S_n, S_p) couple fundamental recombination velocity values, we used the simulation results to calculate τ_{eff} from Equation IV.22. Then, we calculated S_{eff} for each S_n, S_p from Equation IV.17. Figure V.5 draws the results. We can notice that $Seff$ is almost constant at low values of S_n and S_p and grows exponentially at higher values.

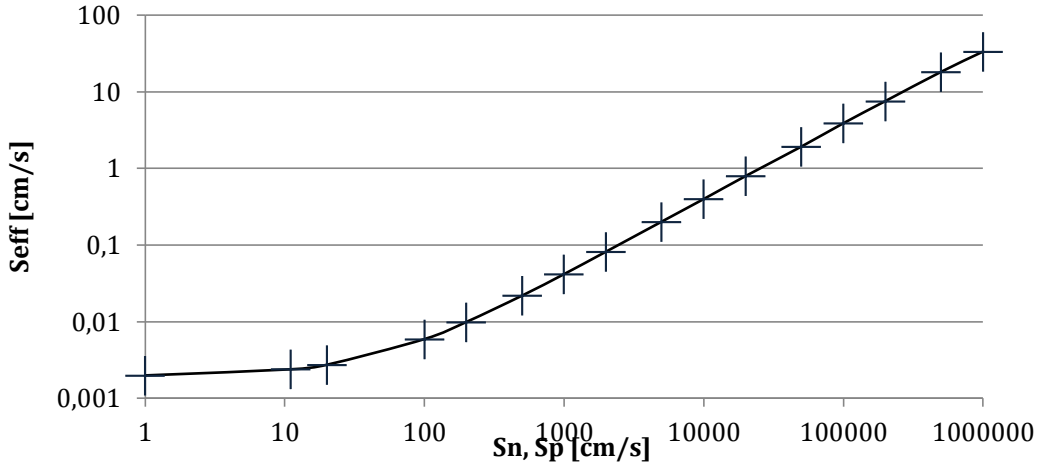

Figure V.5. *Effective surface recombination velocity S_{eff} as a function of surface recombination parameters $\boldsymbol{S_n, S_p}$. Data simulated with PC1D for a wafer thickness $\boldsymbol{w = 400\mu m}$ and a bulk resistivity $\boldsymbol{\rho_b = 2.2\ \Omega.cm}$. Shockley-Read-Hall lifetimes $\boldsymbol{\tau_{p0} = \tau_{n0} = 7ms}$. $\boldsymbol{S_{eff}}$ is calculated at $\boldsymbol{\Delta n = 1 * 10^{15} cm^{-3}}$.*

Experimentally we measured an effective surface recombination velocity $S_{eff} = 4.16\ cm.s^{-1}$. From Figure V.5 we deduce the corresponding surface recombination parameters $S_n = S_p = 1.1 \times 10^5 cm.s^{-1}$. Then, we can simulate the effective lifetime with the software PC1D in order to verify the validity of the method. Figure V.6 draws the measured and simulated lifetimes in function of the excess carrier density.

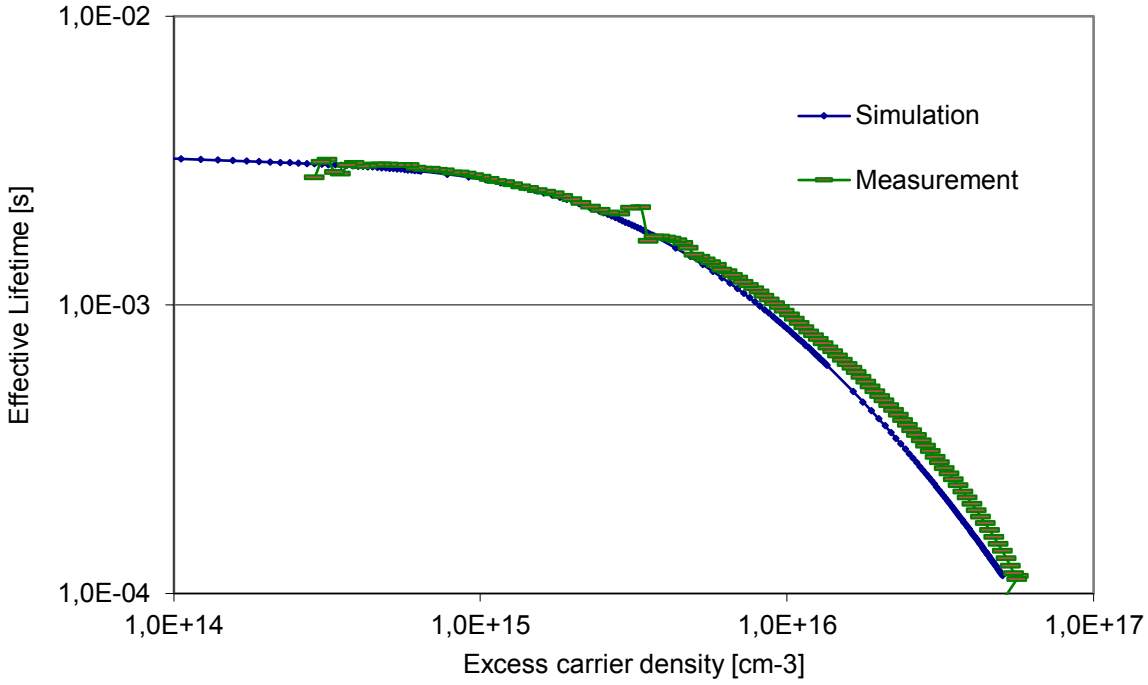

Figure V.6 *Comparison effective lifetime measurement and simulations with PC1D. Parameters are the same as in* **Figure V.5** *with $\boldsymbol{S_n = S_p = 1.1 \times 10^5 cm.s^{-1}}$.*

We can notice that the simulation fits very well the measurements at low injection and slightly overestimates recombination at high injection. Globally we can assume the model is acceptable.

3.5 Front surface recombination velocity without surface charges

Another way to simulate the front surface is to ignore the surface charges and to use $S_n, S_p = S_{eff}$. In our case, we use $S_n, S_p = 4\ cm.s^{-1}$. Figure V.7 draws results of simulations and experiments.

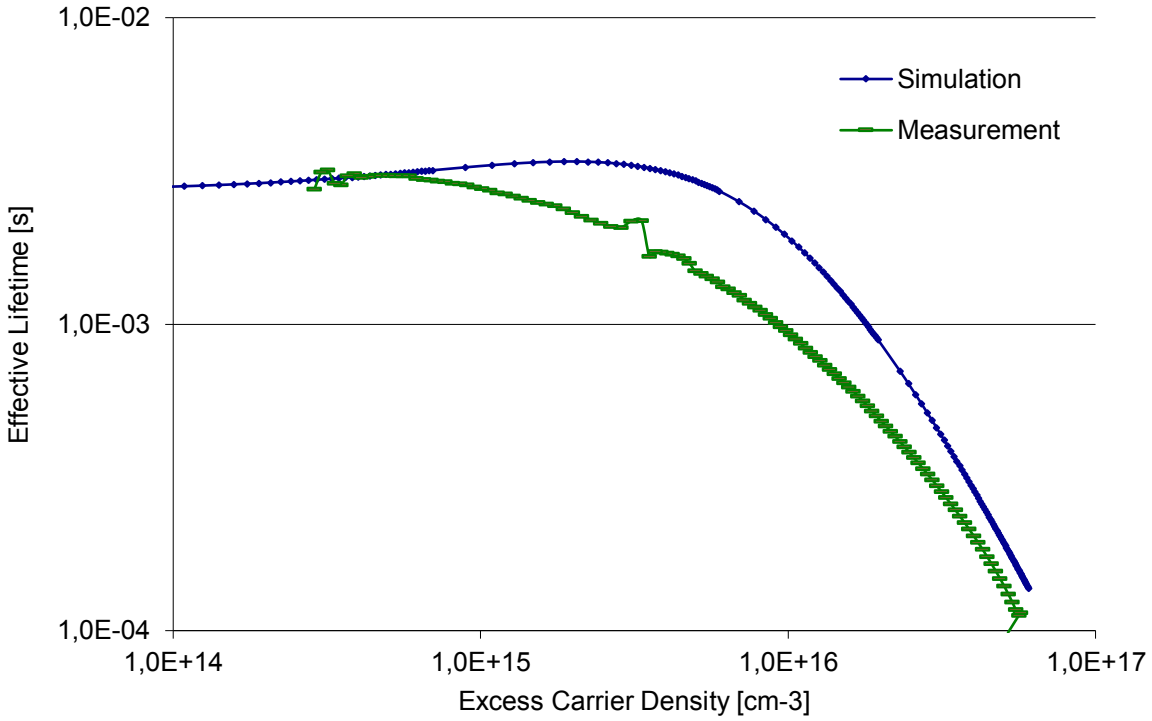

Figure V.7 Comparison effective lifetime measurement and simulations with PC1D. Parameters are the same than for **Figure V.5** with $\mathbf{Qf = 0}$ and $\mathbf{S_n = S_p = 4cm.s^{-1}}$.

This case is not as good as the previous one. The fitting is good enough under $\Delta n = 1 \times 10^{15} cm^{-3}$, however the simulation underestimates recombination at higher injection. Therefore, the most accurate way to simulate the surface recombination is to generate a surface charge at the silicon/aluminium oxide interface. Although this method is easy to perform in one dimension (for instance with PC1D), there are some issues in two dimensions (for instance with ATLAS). This point will be more discussed in the following part.

3.6 Back passivation

The back surface of the cell is passivated by a silicon dioxide (SiO_2) layer grown by wet thermal oxidation. With this method of passivation, the surface recombination velocity depends highly on the surface doping. Hence, it is necessary to consider each part of the cell independently.

3.6.1 Emitter

In our case, the emitter is doped with boron. This case has been studied by P.P. Altermatt et al. [32]. Figure V.8 presents the results of their study.

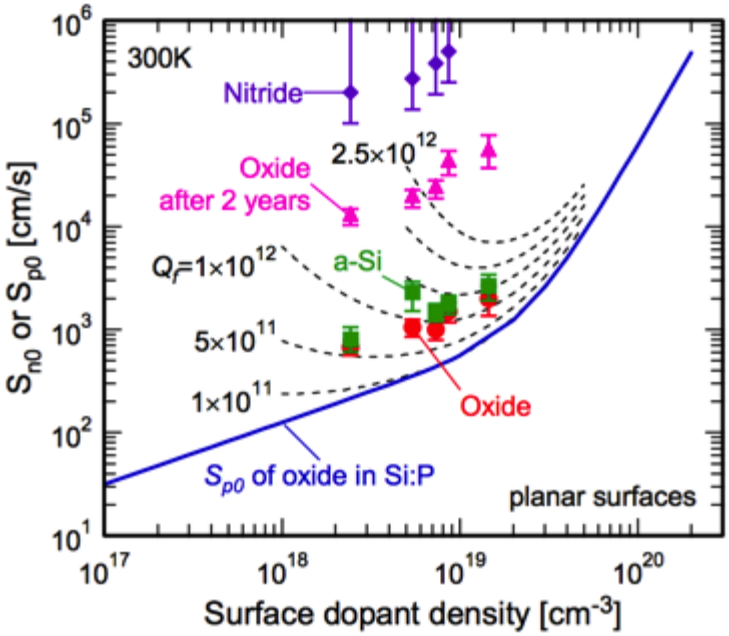

Figure V.8 *Symbols: the surface recombination velocity Sn0 at the boron-diffused emitters, passivated by an oxide, nitride or a-Si/SiNx double-layer, as a function of peak dopant density. The values are extracted by simulating the measured saturation current-density values. Solid line: parameterisation of the average Sp0 at phosphorus-diffused emitters for comparison. Dashed lines: the amplification, due to Qf, of the action of Sn0 on the surface recombination rate* [32].

From those results, it appears that the surface recombination velocity strongly depends of the type of oxide and of its quality. Values for S_n, S_p should be taken between 2000 cm/s and 20.000 cm/s.

3.6.2 Back-surface-field and high doping back-surface-field

In our case, the BSF and BSF+ are doped with phosphorous and passivated with a SiO_2 layer. In this case, it has been shown that S_p is linearly dependant on the peak of concentration of the doped area [33]. This dependence is illustrated in Figure V.9.

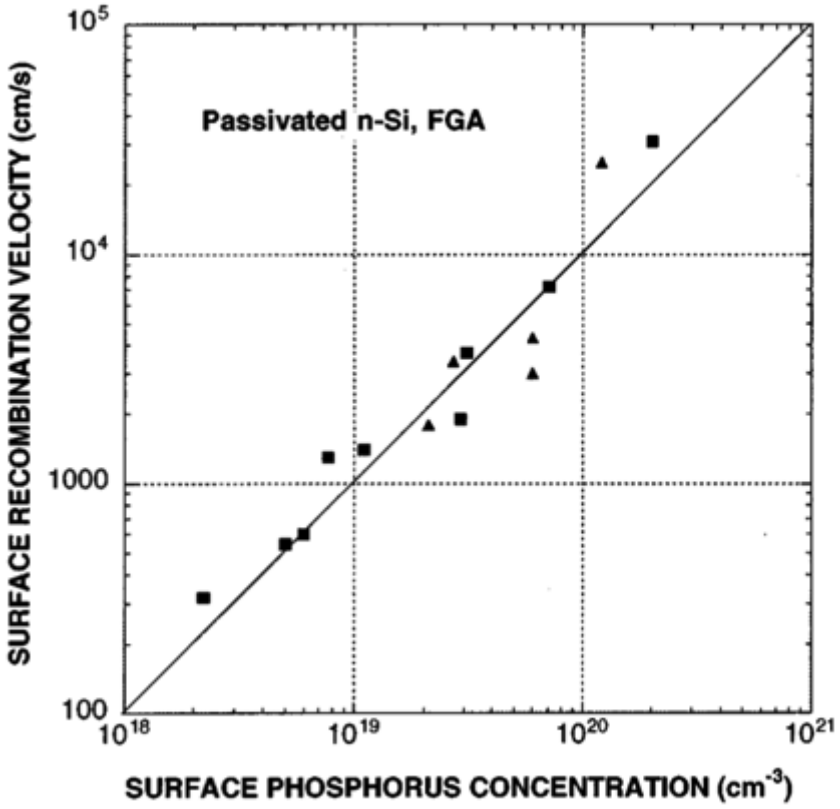

Figure V.9 *Surface recombination velocity (S_p) of oxidized n-type silicon followed by a forming gas anneal as a function of phosphorus concentration [33].*

This dependence can be written with the following formula:

$$\mathbf{S_p = S_0 * \frac{N_{peak}}{N_{Ref}}} \qquad \textbf{Equation V.14}$$

where S_0 and N_{Ref} are parameters depending of the passivation. In the case of thermal oxidation, experiments give us: $N_{Ref} = 10^{-8} cm^{-3}$ and $S_0 = 100\ cm.s^{-1}$.

3.6.3 Metallization

The last case is the interface between the silicon and the metallization. In our case, the metallization is a square point contact aluminium alloy of 50µm width. A similar case has been studied by Jens Müllera et al. [34].

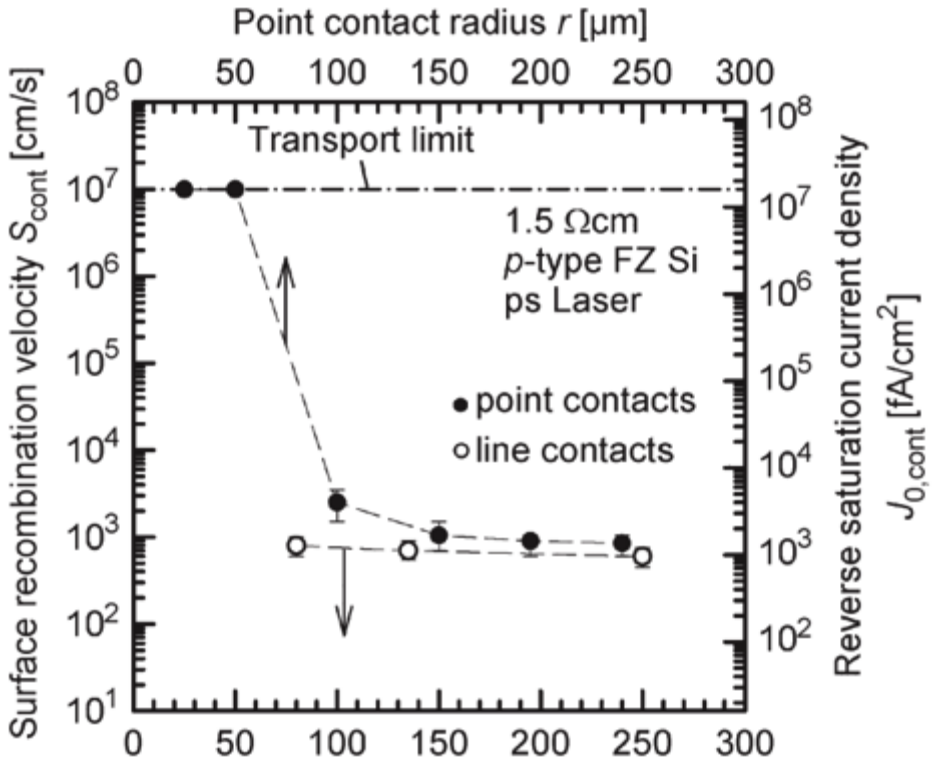

Figure V.10 *Contact recombination velocity S_{cont} and contact reverse saturation current density $J_{0,cont}$ at (closed circles) point contacts as a function of the contact radius and (open circles) line contacts as a function of the line width, measured on wafers of 1.5-Ωcm resistivity. The lines are guides to the eye. The thermal velocity is equal to the transport limit.*[34].

Figure V.10 draws results of Jens Müllera et al. experiments. In our case the surface recombination velocity is limited by the thermal velocity, $v_{th} = 1 \times 10^7 cm/s$.

3.6.4 Summary

Table V.8 summarises the surface recombination parameters for the rear surface of the solar cell.

Area	BSF	BSF+	Emitter	Metallization
S_n, S_p (cm/s)	900	6x10^3	2x10^3 – 2x10^4	10^7

Table V.8 *Summary table of surface recombination velocity parameters*

3.7 Internal reflectance of the back-side

The backside of the cell is composed of 3 different interfaces. Each interface has a different reflectance. The three cases have been studied in the literature and reflectance at normal incidence are given in Table V.9 [35, 36].

Interface	Silicon/SiO_2/Aluminium	Silicon/SiO_2/Air	Silicon/Aluminium
Reflectance	94%	25%	86%

Table V.9 *Summary of reflectance at the rear surface .*

Considering the structure presented in Figure V.1 we calculate the total reflectance of the rear side using the following equation:

$$\mathbf{R_{tot}} = \frac{\mathbf{2} * \boldsymbol{w_{elec.}} * (\mathbf{86} - \mathbf{94}) + \boldsymbol{gap_{elec.}} * (\mathbf{25} - \mathbf{94}) + \boldsymbol{x_{max}} * \mathbf{94}}{\boldsymbol{x_{max}}} \qquad \textbf{Equation V.15}$$

It results: $R_{tot} = 83\%$. However, this value is underestimated. Indeed, in the cases of black-silicon or random pyramids, the incoming rays are surely deflected from the normal incident and a total internal reflection could occur. Therefore, it seems reasonable to increase this value. From now on, we will use $R_{tot} = 90\%$.

3.8 Meshing

The finite element mesh is very important in numerical simulation. A finer mesh commonly gives more accurate results however the simulation takes more time. One method to evaluate the correct fineness of the mesh is to perform several simulations with a finer mesh every next simulation. Then, we investigate the convergence of the simulations depending on the fineness.

3.8.1 Meshing with surface charge

First, we tried simulations with a surface charge $QF = 5 \times 10^{12} cm^{-3}$. The simulated cell is plotted with the software Silvaco Tonyplot in Figure V.11. The front side is on the top of the figure. On the bottom, we can observe the different doped areas. The net doping scale is logarithmic.

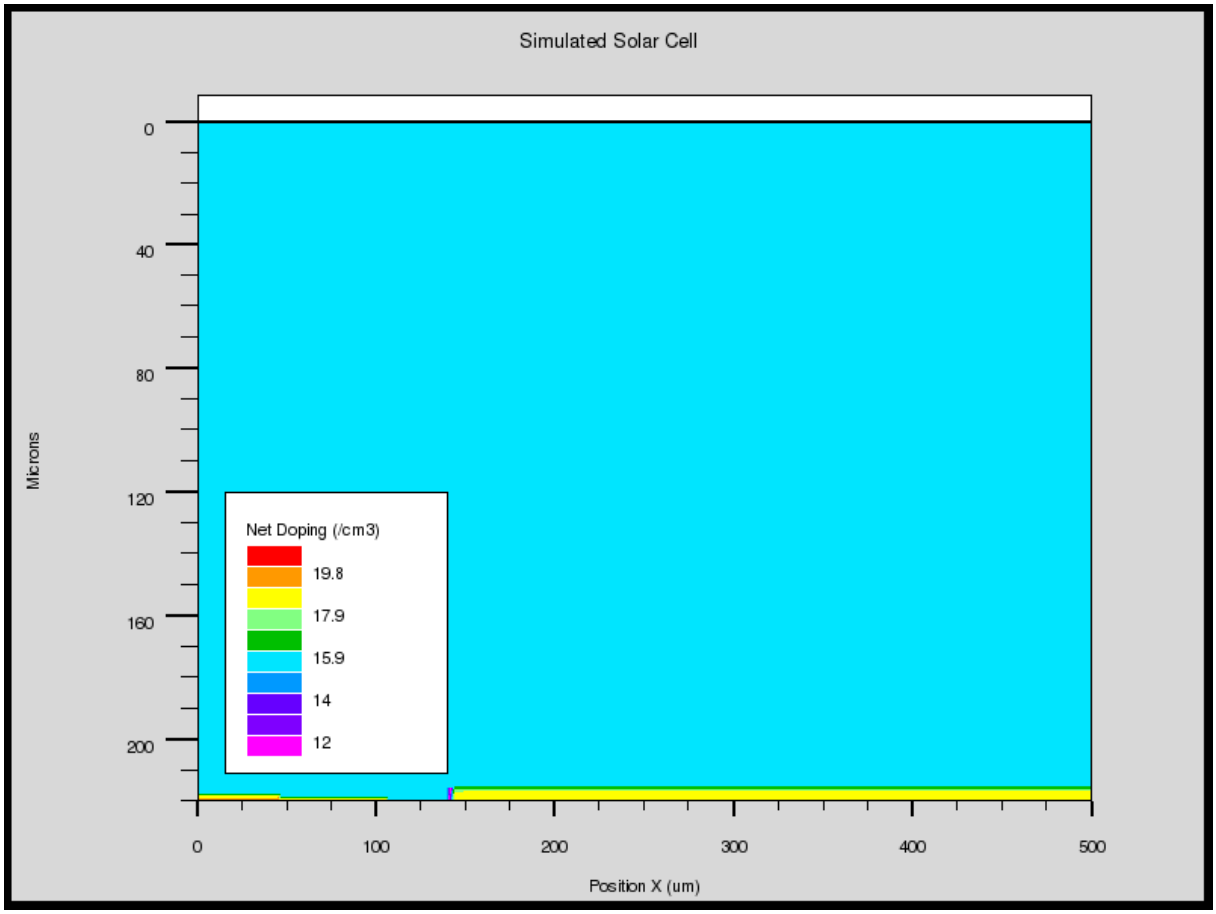

Figure V.11 *Simulated cell plotted with Silvaco Tonyplot*

The reference mesh, with an arbitrary fineness, is done and is drawn in Figure V.12.

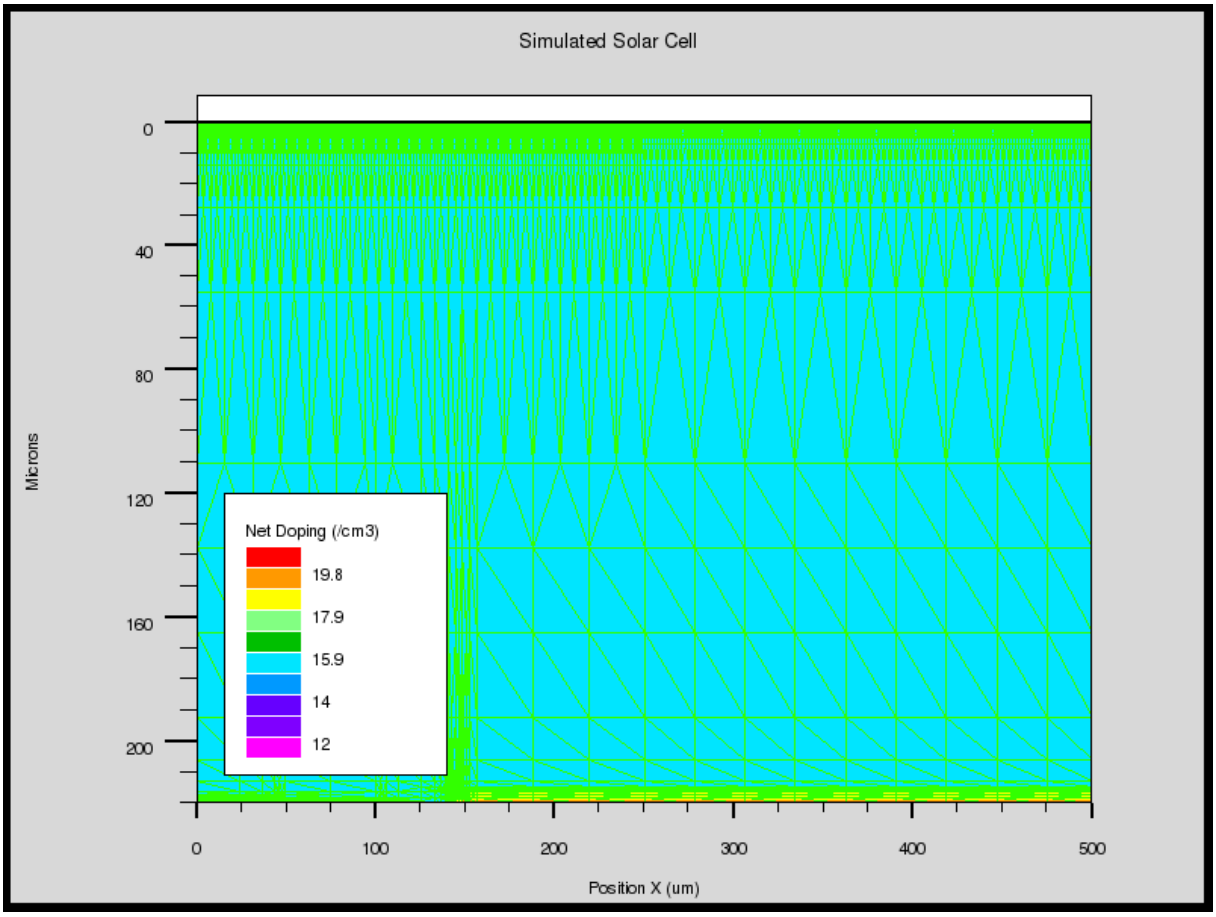

Figure V.12 *Reference mesh of the simulated cell with surface charge*

The mesh is made finer at high doping concentration gradient areas and near the front surface with high surface charge density for the purpose of increasing the accuracy. From here, we performed several simulations increasing the fineness every next simulation.

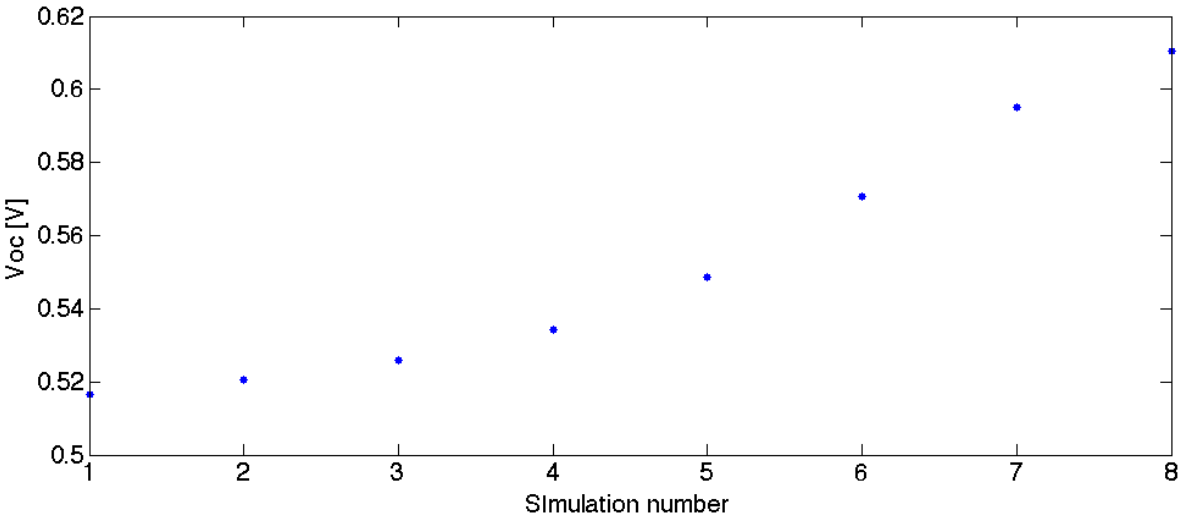

Figure V.13 *Open-circuit voltage function of the simulation number. The fineness of the cell is multiplied by two every next simulation starting from the simulation number 1.*

In Figure V.13 it appears that the simulation does not converge when the fineness increases. Looking at the shape of the curve, it seems reasonable that the simulation would converge if we increased the fineness more. However, we already reached the ATLAS node limitation. In other words, we cannot use the model with surface charges at the front interface since the results are not accurate enough. Despite the poor accuracy of the model without surface charges and with $S_n = S_{eff}$ to simulate the surface front recombination, we will use it in our simulations since it generates converging solutions (c.f. following chapter).

3.8.2 Meshing without surface charge

The same method is used without surface charge. In this case, the mesh does not need to be highly fine at the front surface and the simulations are significantly easier to perform. Figure V.14 draws the open-circuit voltage function of the simulation number and Figure V.15 the efficiency. The x-axes is chosen arbitrarily and cannot be compared with the x-axes in Figure V.13.

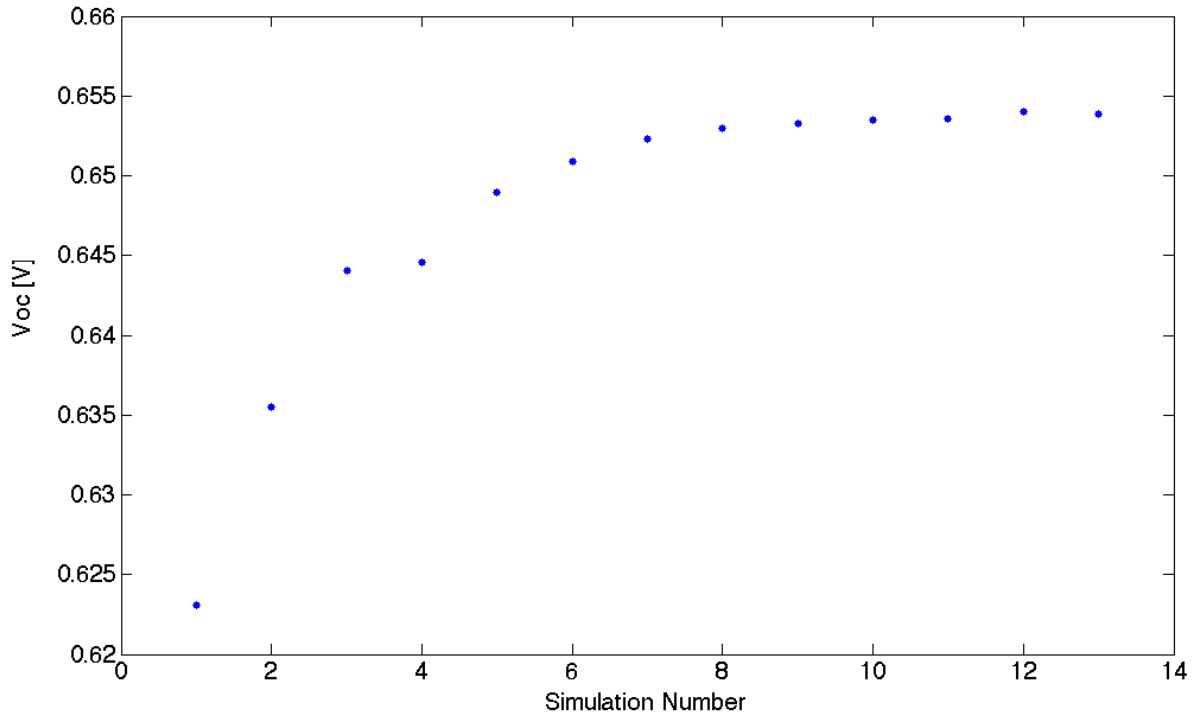

Figure V.14 *Open-circuit voltage function of the simulation number. The fineness of the cell is multiplied by two every next simulation starting from the simulation number 1.*

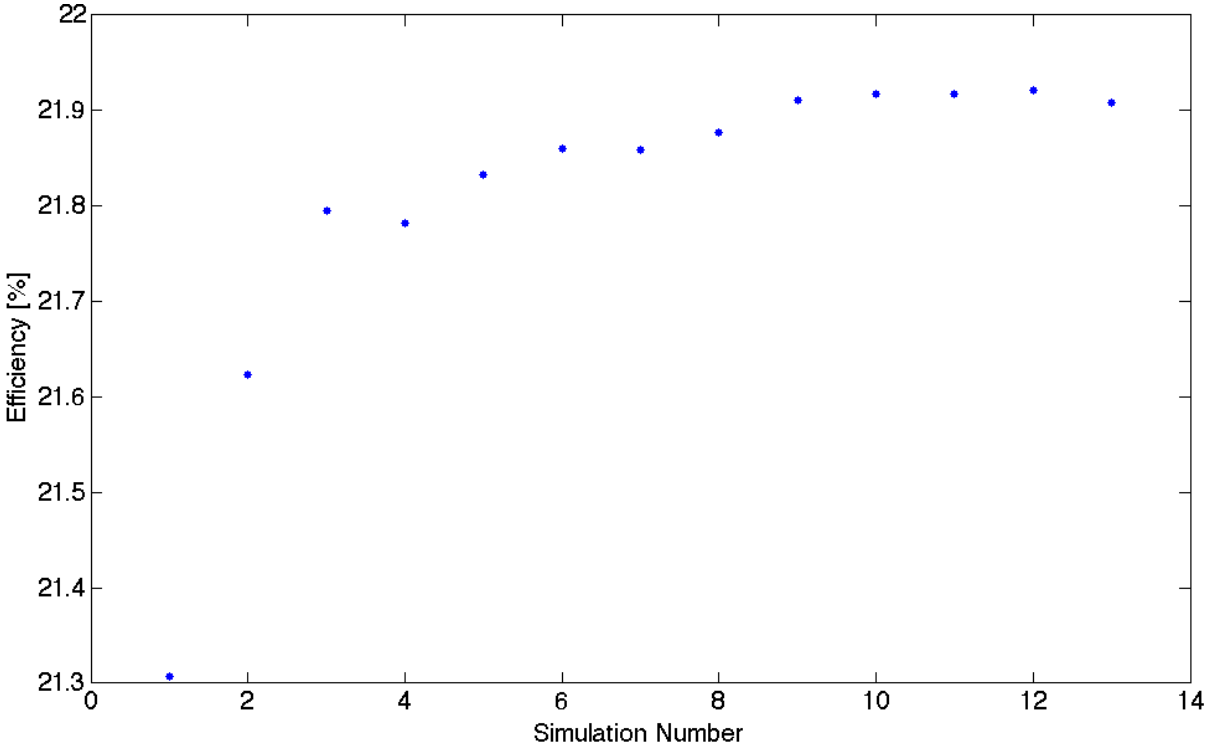

Figure V.15 *Efficiency function of the simulation number. The fineness of the cell is multiplied by two every next simulation starting from the simulation number 1.*

From Figure V.14 and Figure V.15, we conclude that the simulation solutions converge with the fineness of the mesh. The eighth simulation gives us a good compromise between speed and accuracy. From now on we will use the corresponding mesh for every simulation.

4 Discussion of the model

For the purpose of determining the accuracy of the model, we compare experiments with simulation. Current-voltage (IV) characteristics are compared in the dark and under illumination.

4.1 Experimental data

Float-Zone (FZ) <100> n-type wafers with bulk resistivity of ~1.4 Ohms.cm and a thickness of 250µm were used as substrates. Point-contact IBC solar cells have been produced on those substrates in the micro- and nanotechnology laboratory of the *Universitat Politècnica de Catalunya Barcelona* (UPC Barcelona). Four cells with different emitter coverage have been designed following the structure presented in Figure V.1. The top surface is textured with random pyramids as anti-reflecting layer.

4.2 Simulation in the dark

We measured the current-voltage (IV) characteristics of the processed cell in the dark. The current-voltage (IV) characteristics in the dark are drawn on Figure V.17 for both the processed and the simulated cell. Simulations are performed with parameters discussed in the previous part of this thesis.

The surface recombination velocities at the emitter surface and contact resistance were chosen to fit the experimental IV curve in the dark at high voltage. It results in surface recombination velocities equal to 8000cm/s and in contact resistances of 0.18 ohms at each electrode. It appears that an asymmetry in recombination parameters at the surface of the gap on the rear side gives a better fitting of the experimental curve at low voltage.

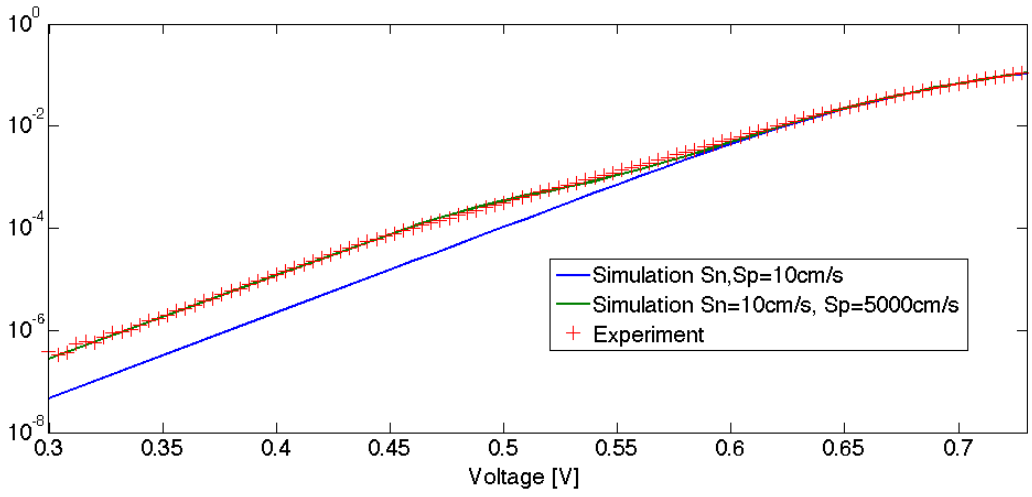

Figure V.16 *IV characteristics of simulated cells and experimental cell in the dark. Sn and Sp are the electron and hole recombination parameters at the surface of the gap.*

From now on, we will use respectively S_nGap=10cm/s and S_pGap=5000cm/s as electron and hole surface recombination velocities at the surface of the gap, S_nEmitter=8000cm/s and S_pEmitter=8000cm/s as electron and hole surface recombination velocities at the surface of the emitter and $R_{Contact}$=0.18 ohms as contact resistance at each electrode.

4.3 Simulation under illumination

In this section, we kept the same parameters as in the dark and we added the weighted spectrum corresponding to the random pyramids surface. The processed cell is characterised under AM1.5G spectrum.

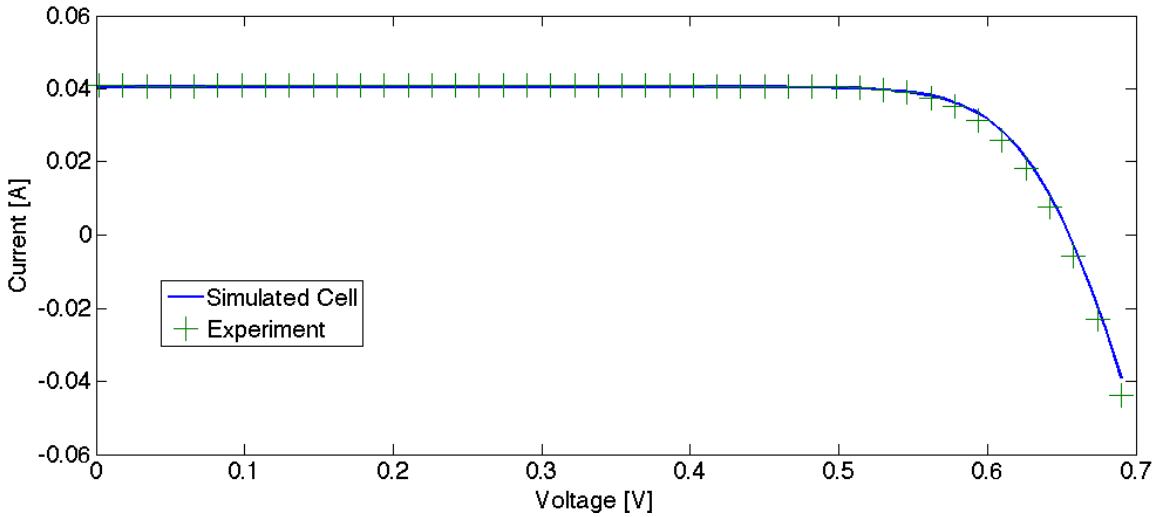

Figure V.17 *IV characteristics of (blue line) simulated cell and (green crosses) experimental cell under AM1.5G spectrum.*

The simulation fits very well the experiments. Table V.10 compares the main characteristics of the experimental and the simulated cell.

	Voc (V)	Isc (mA)	FF (%)	Efficiency (%)
Simulation	0.654	40.5	80.7	21.37
Experiment	0.651	40.9	79.7	21.3
Relative Error	0.4%	0.9%	1.2%	0.3%

Table V.10 *Comparison between the experimental cell and simulated cell.*

The maximum relative error is 1.2%. This value is low enough to accept the model.

VI. Impact of model parameters on black silicon solar cell efficiency

In this section, we first compare simulations between random pyramids and black-silicon. In the subsequent sections, every simulation is performed with black-silicon as anti-reflection layer. In each sub-section, one simulation parameter is studied independently from the others. All other simulation parameters are set to the reference values discussed in the previous section and presented in appendix 2.

1 Black-silicon versus random pyramids

Black-silicon and random pyramids were simulated by using a weighted spectrum as incoming light. The method is described in sub-section 0. Figure VI.1 draws the IV characteristics of both simulations.

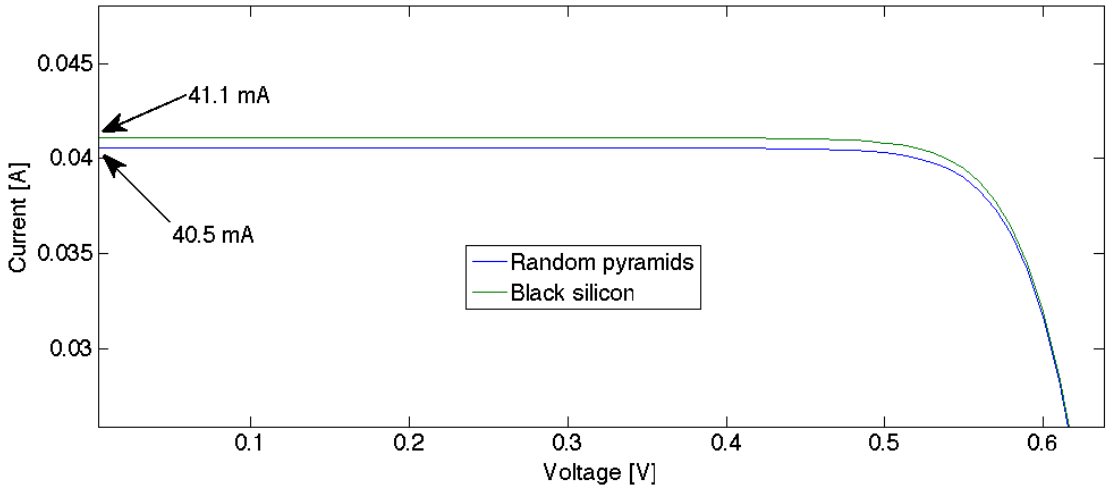

Figure VI.1 *IV characteristics, black-silicon versus random pyramids.*

As expected, the short-circuit current is increased with black-silicon. This effect is a direct consequence of the lower reflectance of black-silicon. The cells' main characteristics are presented in Table VI.1.

	Voc (V)	Isc (mA)	FF (%)	Efficiency (%)
Random pyramids	0.654	40.5	80.7	21.37
Black-silicon	0.655	41.1	80.6	21.7

Table VI.1 *Comparison black-silicon versus random pyramids*

The efficiency of the black-silicon cell is 0.3% higher than the random pyramids cell. This gain is mainly due to the increase of short-circuit current. It may seem low,

however b-Si brings other advantages compared to random pyramids, such as a low reflectance over a large range of incident angles.

2 Front surface recombination velocity

In this section, we study the impact of the front surface recombination in b-Si cells so the b-Si spectrum is used in the input of the model. S_n and S_p are set equals. Since the bulk is doped with phosphorous, the impact of S_n is negligible compare to the impact of S_p (c.f. Equation I.9). Figure VI.2 and Figure VI.3 draw respectively Voc and Isc function of the front surface recombination velocity parameters.

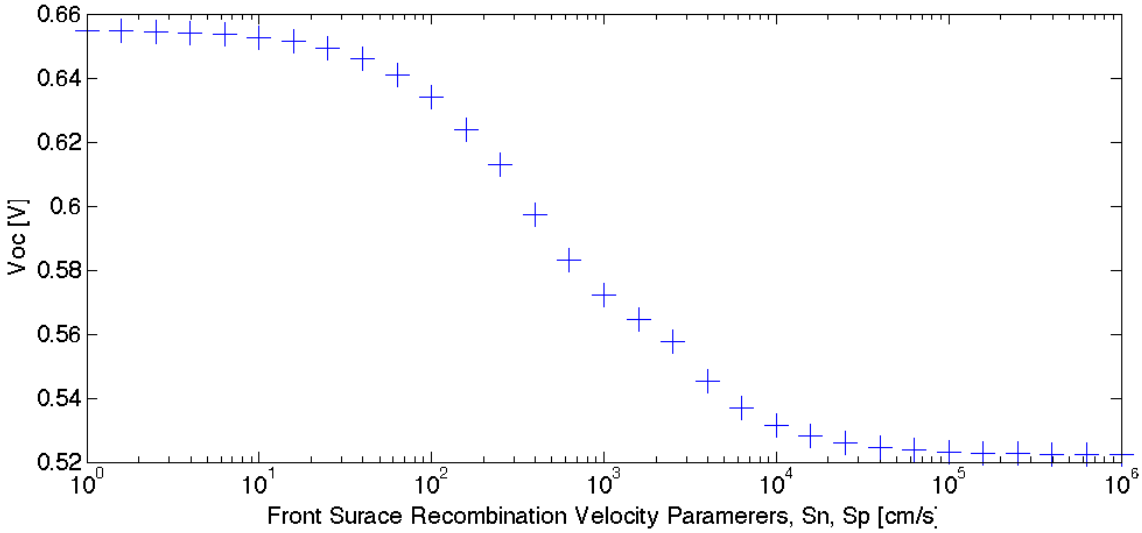

Figure VI.2 *Impact of the front surface recombination velocity on the open-circuit voltage.*

The higher Sn and Sp, the higher the recombination rate at the surface is and the lower the Voc becomes. Indeed, with a high recombination rate at the surface, fewer charge carriers reach the pn-junction.

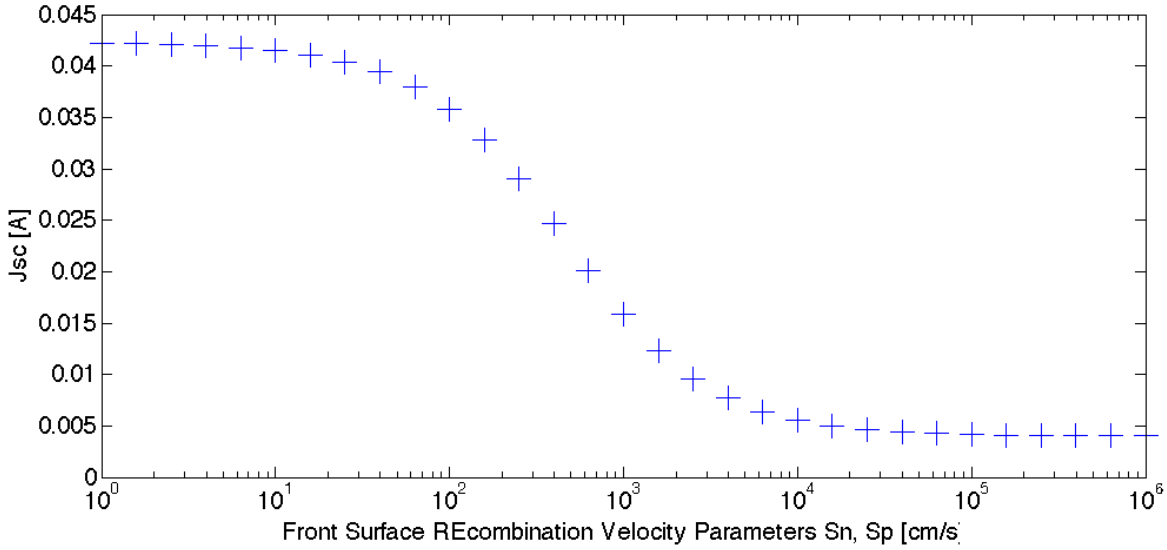

Figure VI.3 *Impact of the front surface recombination velocity on Isc.*

Isc decreases when the front surface recombination velocity increases. The effect is very important since the maximum photogeneration area is near the front surface. At high values of Sn, Sp, Isc converge to a low but non-zero current. This low current corresponds to the carriers photo-generated near the junction that are collected before being recombined.

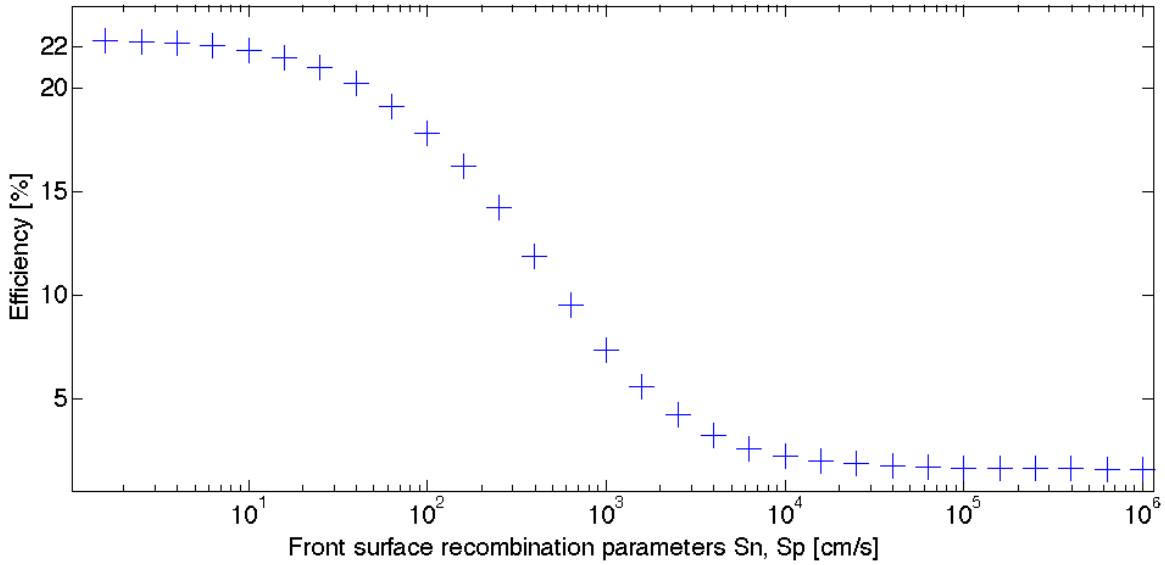

Figure VI.4 *Impact of the front surface recombination velocity on the efficiency.*

Figure VI.4 draws the cell efficiency function of Sn, Sp. As expected, the curve follows the same shape as Isc and Voc. Indeed, when decreasing Voc and Isc, necessarily the efficiency decreases. With the experimental front passivation ($S_n, S_p \approx 5\ cm\ s^{-1}$), the efficiency is near the maximum and decreasing the front surface recombination velocity would be worthless.

3 Emitter surface recombination velocity

In this chapter, we study the impact of the emitter surface recombination velocity. S_n and S_p are set equals. Since the emitter is highly doped with boron, the impact of S_p is neglectible compare to the impact of S_n (c.f. Equation I.9). Figure VI.5 draws the open-circuit voltage function of the emitter surface recombination velocity parameters.

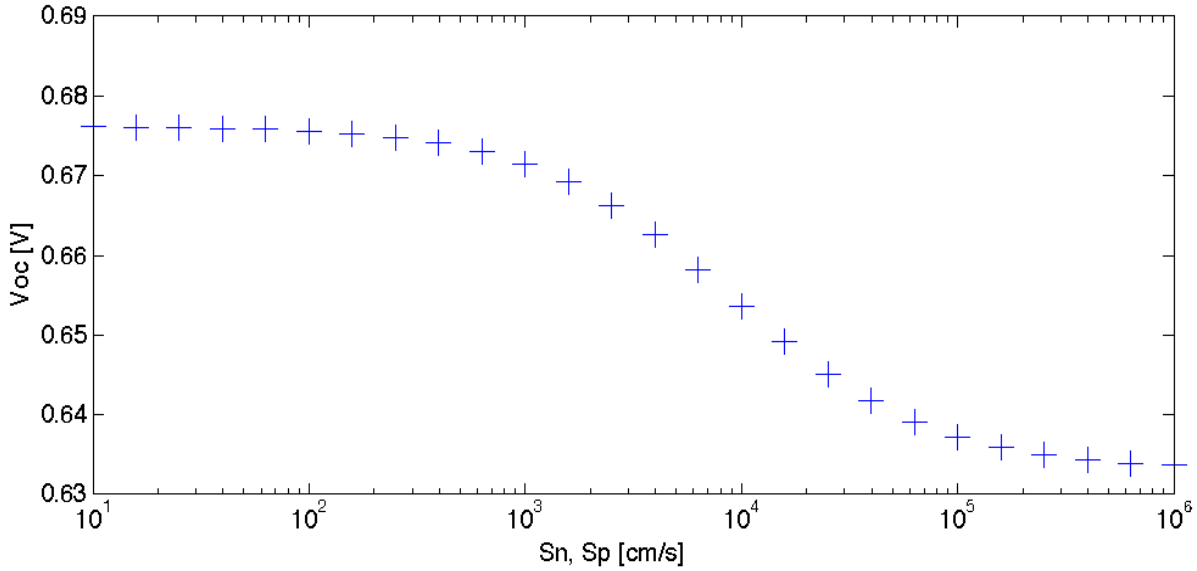

Figure VI.5 *Impact of the emitter surface recombination velocity on Voc.*

First we can notice that Voc decreases significantly over Sn, Sp=1000cm/s. Unfortunately, with a silicon oxide passivation layer, Sn, Sp are over 2000cm/s (c.f. Figure V.8). A better emitter passivation would be useful to significantly increase the open-circuit voltage of the cell.

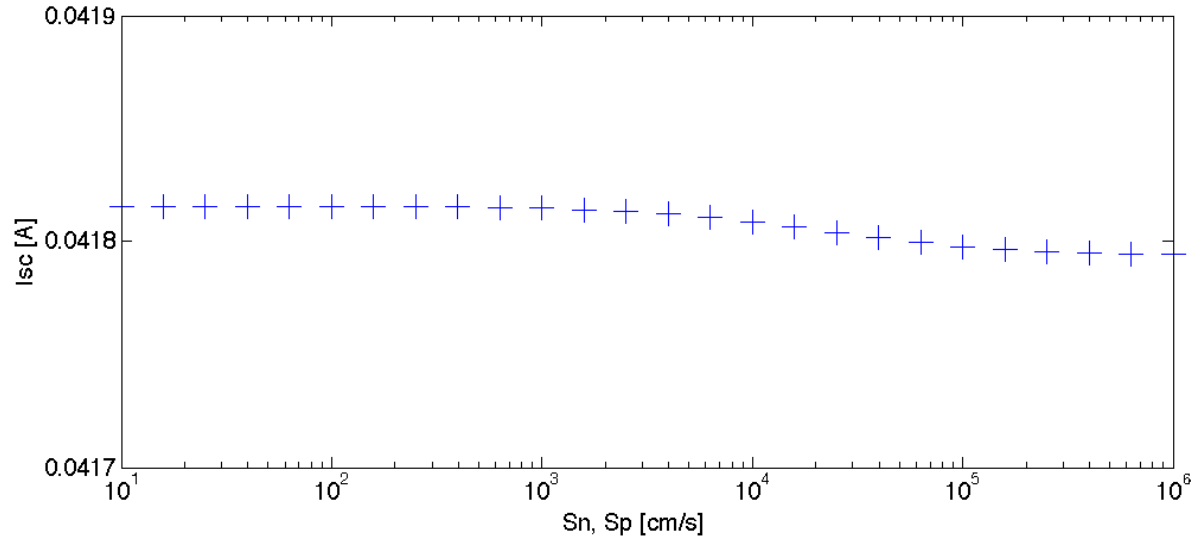

Figure VI.6 *Impact of the emitter surface recombination velocity on Isc.*

The impact on Isc is presented in Figure VI.6. Considering the scale of the y-axis, we observe that the emitter surface recombination velocity does not influence Isc.

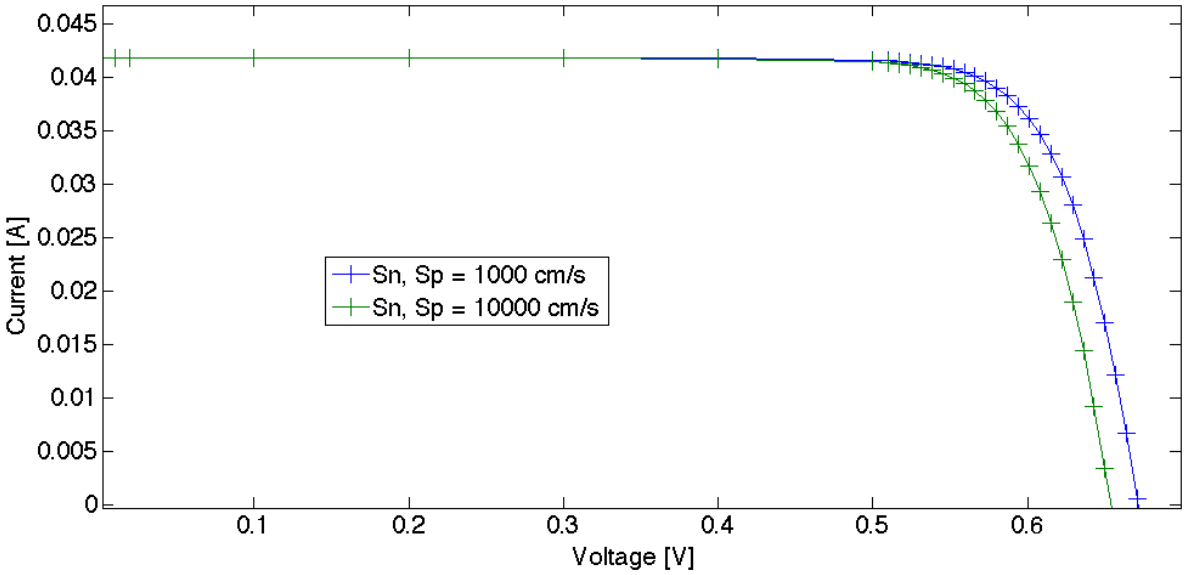

Figure VI.7 *IV characteristics of the simulated cell with emitter surface recombination parameters Sn, Sp=1000cm/s (blue line) and Sn, Sp=10000cm/s (green line).*

Figure VI.7 draws the IV characteristics of the simulated cell with emitter surface recombination parameters Sn, Sp=1000cm/s and Sn, Sp=10000cm/s. The shape of the green curve in comparison to the blue curve is typical of an augmentation of dark saturation current.

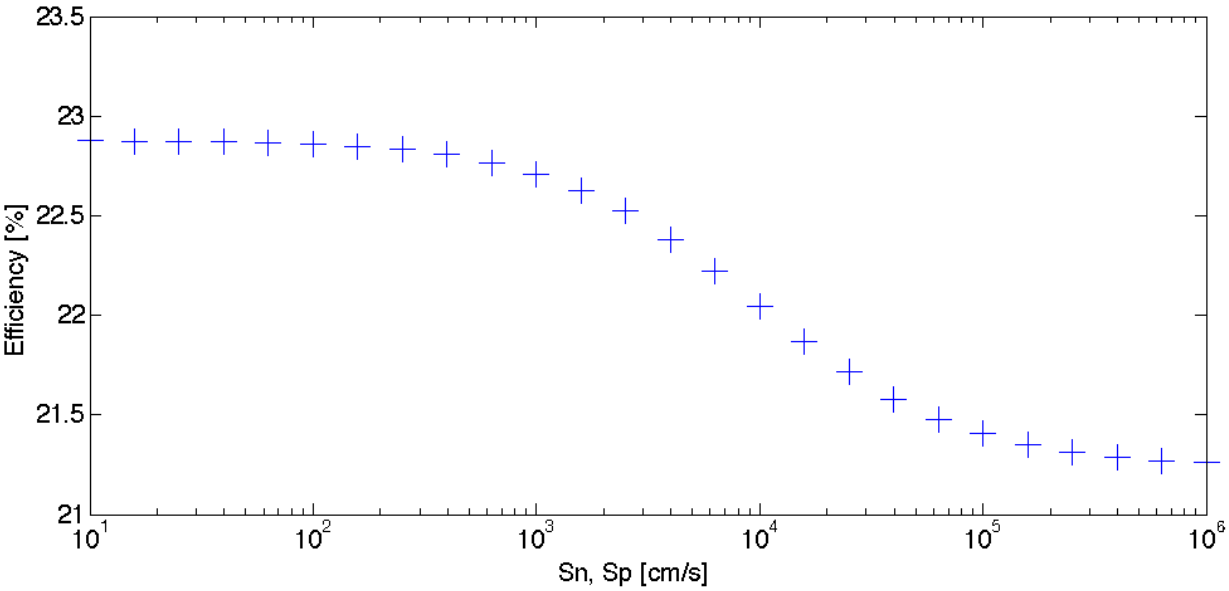

Figure VI.8 *Impact of the emitter surface recombination velocity on the efficiency.*

The impact on the efficiency drawn in Figure VI.8 Once again, the shape follows the shape of the Voc curve. It appears that a better passivation of the emitter could bring the cell efficiency to a significant higher level.

Conclusion

In this thesis, we have simulated n-type IBC solar cells with black silicon on the front surface, passivated with Al_2O_3 layer grown by ALD.

First, we focused on the front surface recombination velocity. We were able to simulate the aluminium oxide passivation in one dimension using PC1D software and we compared the simulation with minority carrier lifetime experiments. A good agreement of the experiments was obtained using a front surface charge density $Qf = 5.10^5 cm^{-3}$ and surface recombination parameters $Sn = Sp = 1.1 \times 10^5 cm.s^{-1}$. However, the maximum node number of ATLAS appeared to be too low to simulate the surface charge density properly in the case of IBC cells. For the next simulation we used $Sn = Sp = 4\ cm.s^{-1}$ and $Qf = 0$. This model is less accurate than the previous but required fewer nodes.

Then, an n-type IBC cell with random pyramids anti-reflection layer was simulated. The low Voc obtained experimentally suggests a low passivation quality of the emitter. By fitting the simulations with the experiments, we obtained the emitter surface recombination velocities $S_n = S_p \approx 8000\ cm.s^{-1}$. Using this latter value, the simulated solar cell characteristics agreed with the experimentally obtained ones made at UPC Barcelona with an accuracy of 1.2 %.

Then, we studied the impact of adding black-silicon front surface to replace the conventional random pyramids on the solar cell characteristics. It was found out that, at normal incidence, black-silicon would increase the short circuit current of 6mA and the efficiency of 0.3%.

The front passivation with Al_2O_3 grown by ALD generates an effective surface recombination velocity $S_{eff} \approx 5\ cm.s^{-1}$. According to the simulations, a better passivation of the front surface would not be beneficial to the efficiency.

The emitter surface recombination velocity has a high impact on Voc. Improving the emitter passivation could increase the open-circuit voltage of 21mV and the efficiency of 1.1% absolute.

In conclusion, ATLAS is a very powerful tool to simulate silicon solar cell. In this work we created an accurate model to simulate IBC cells. From now, this model can be used to optimize each parameter of the cell.

,

Appendix 1: Silvaco ATLAS code

```
go ATLAS

set maillage=0.7

#BULCK
set xmax=500
set ymax=220
set tau=0.010
set bulkRes=1.4

#DOPED AREAS
set gap=40

set wBSF=210
set yBSF=1.1
set BSFNpeak=0.9e19

set wEmitter=$xmax*2-$wBSF-$gap*2
set yEmitter=5
set EmitterNpeak=1e19

set wBSFHigh=90
set yBSFHigh=2.3
set BSFHighNpeak=6e19

#PASSIVATIONS
set Nref=1e18
set VElectrode=1e7

set SFront=6
set SNBack=10
set SPBack=5000
set SBackBSF=100*$BSFNpeak/$NRef
set SBackBSFHigh=100*$BSFHighNpeak/$NRef
set SBackEmitter=8000

#ELECTRODES
set wElectrode=50
set gapElectrode=80

#MESH
set w=1e8/$xmax
set BackReflectance = 0.9
set FrontReflectance = 1

mesh width=$w

x.mesh location=0                    spacing=0.5
x.mesh location=$wBSF/2              spacing=2
x.mesh location=$xmax/2              spacing=50
x.mesh location=$xmax-$wElectrode/2  spacing=2
x.mesh location=$xmax                spacing=0.5
```

```
y.mesh loc=0       spacing=0.0001
y.mesh loc=$ymax/2 spacing=$ymax/30
y.mesh loc=$ymax   spacing=0.05

ELIMINATE COLUMNS X.MIN=0 X.MAX=$wBSF/2+$Gap-20 Y.MIN=0.0 Y.MAX=$ymax-5
ELIMINATE COLUMNS X.MIN=0 X.MAX=$wBSF/2+$Gap-10 Y.MIN=0.0 Y.MAX=$ymax-10
ELIMINATE COLUMNS X.MIN=0 X.MAX=$wBSF/2+$Gap-5  Y.MIN=0.0 Y.MAX=$ymax-15
ELIMINATE COLUMNS X.MIN=0 X.MAX=$wBSF/2+$Gap    Y.MIN=0.0 Y.MAX=$ymax-20
ELIMINATE COLUMNS X.MIN=$xmax-$wElectrode/2-5  X.MAX=$xmax Y.MIN=0.0
Y.MAX=$ymax-5
ELIMINATE COLUMNS X.MIN=$xmax-$wElectrode/2-15 X.MAX=$xmax Y.MIN=0.0
Y.MAX=$ymax-12
ELIMINATE COLUMNS X.MIN=$xmax-$wElectrode/2-35 X.MAX=$xmax Y.MIN=0.0
Y.MAX=$ymax-25

region num=1 material=Silicon x.min=0 x.max=$xmax y.min=0 y.max=$ymax

electrode num=1 name=cathode material=Aluminium LENGTH=$wElectrode/2   LEFT
y.min=$ymax-0.01 y.max=$ymax
electrode num=2 name=anode material=Aluminium LENGTH=$wElectrode/2
RIGHT y.min=$ymax-0.01 y.max=$ymax

doping region=1 uniform n.type resist=$bulkRes x.min=0.0 x.max=$xmax
y.min=0 y.max=$ymax

#emitter
doping region=1 gaus p.type start=$ymax junction=$ymax-$yEmitter
concentration=$EmitterNpeak RATIO.LATERAL=0.7 x.min=$xmax-$wEmitter/2
x.max=$xmax y.min=$ymax y.max=$ymax

#baseHigh
doping region=1 gaus n.type start=$ymax junction=$ymax-$yBSFHigh
concentration=$BSFHighNpeak RATIO.LATERAL=0.7 x.min=0 x.max=$wBSFHigh/2
y.min=$ymax y.max=$ymax

#base
doping region=1 gaus n.type start=$ymax junction=$ymax-$yBSF
concentration=$BSFNpeak RATIO.LATERAL=0.7 x.min=$wBSFHigh/2 x.max=$wBSF/2
y.min=$ymax y.max=$ymax

save outfile=init.str master

Go DevEdit
load file.name=init.str type=str
base.mesh height=20*$maillage width=40*$maillage

bound.cond !apply max.slope=28 max.ratio=300 rnd.unit=0.001
line.straightening=1 align.points when=automatic

imp.refine imp="Device Potential" scale=linear sensitivity=0.5
imp.refine imp="N Carriers"  scale=log
imp.refine imp="Net Doping"  scale=log
imp.refine min.spacing=0.01*$maillage

constr.mesh max.angle=90 max.ratio=300 max.height=10000 max.width=10000
min.height=0.0001 min.width=0.0001
constr.mesh type=Semiconductor default
constr.mesh type=Insulator default max.angle=179
```

```
constr.mesh type=Metal default max.angle=178
constr.mesh type=Other default

constr.mesh id=1 x1=0        y1=0                x2=$xmax y2=10*$maillage
default  max.height=5*$maillage max.width=10*$maillage
constr.mesh id=2 x1=0        y1=$ymax-1          x2=50    y2=$ymax
default  max.height=3*$maillage max.width=5*$maillage
constr.mesh id=3 x1=$xmax-50 y1=$ymax-4*$maillage x2=$xmax y2=$ymax
default  max.height=3*$maillage max.width=5*$maillage

Mesh Mode=MeshBuild
save type=master file.name=refined.str
quit
go atlas

mesh infile=refined.str master.in width=$w

#Front with weighted spectrum
material reg=1 taun0=$Tau taup0=$Tau NSRHN=1e16 NSRHP=1e16

models  fermidirac bgn ccsmob consrh fldmob auger optr temperature=300
print

contact name=cathode  surf.rec vsurfn=$VElectrode vsurfp=$VElectrode
resistance=0.19 OHMS
contact name=anode    surf.rec vsurfn=$VElectrode vsurfp=$VElectrode
resistance=0.19 OHMS

#MATERIAL RECOMBINATION
interface S.X S.N=$SFront       S.P=$SFront        x.min=0
x.max=$xmax                  y.min=-1     y.max=1

interface S.X S.N=$SBackBSFHigh S.P=$SBackBSFHigh   x.min=$wElectrode/2
x.max=$wBSFHigh/2         y.min=$ymax-1 y.max=$ymax+1
interface S.X S.N=$SBackBSF     S.P=$SBackBSF       x.min=$wBSFHigh/2
x.max=$wBSF/2             y.min=$ymax-1 y.max=$ymax+1
interface S.X S.N=$SNBack       S.P=$SPBack         x.min=$wBSF/2
x.max=$wBSF/2+$gap        y.min=$ymax-1 y.max=$ymax+1
interface S.X S.N=$SBackEmitter S.P=$SBackEmitter   x.min=$wBSF/2+$gap
x.max=$xmax-$wElectrode/2 y.min=$ymax-1 y.max=$ymax+1

#MATERIAL REFLECTION
interface  optical reflect=$BackReflectance  x.min=0    x.max=$xmax
y.min=$ymax y.max=$ymax
interface  optical reflect=$FrontReflectance x.min=0    x.max=$xmax
y.min=0     y.max=0

#MODEL
METHOD NEWTON
output e.field opt.intens con.band val.band photogen recomb traps
e.mobility h.mobility u.auger u.srh u.trap

#Beam with weighted spectrum
beam number=1 x.origin=0 y.origin=-1 angle=90
power.file=spectrumWeighted.txt min.window=0 max.window=$xmax REFLECTS=12
BACK.REFL min.power=1e-4

solve init
save outfile=init.str
```

```
solve b1=1e-10
solve b1=1e-9
solve b1=1e-8
solve b1=1e-7
solve b1=1e-6
solve b1=1e-5
solve b1=1e-4
solve b1=1e-3
solve b1=1e-2
solve b1=0.1
solve b1=0.3
solve b1=1

save outfile=strc.str master

log outfile=IV.log
solve vanode=0 vstep=0.01 vfinal=0.02 name=anode      index.check
solve vanode=0.1 vstep=0.1 vfinal=0.5 name=anode      index.check
solve vanode=0.51 vstep=0.007 vfinal=0.680 name=anode index.check
log close

#RESULT ANALYSIS
extract init infile="IV.log"
extract name="Voc" x.val from curve(v."anode", i."anode") where y.val=0
extract name="Jsc" y.val from curve(v."anode", i."anode") where x.val=0
extract name="Pmax" min(v."anode"*i."anode")
extract name="Vmax" x.val from curve(v."anode", v."anode"*i."anode") where
y.val=max(v."anode"*i."anode")

set Efficiency= $"Pmax"/($"w"*$"xmax"*0.10004*0.00000001)*100
set fill_factor= $"Pmax"/($"Voc"*$"Jsc")
set Jsc_cm2= ($"Jsc"/($"w"*$"xmax"*0.00000001))
set Jmp= $"Pmax"/($"xmax"*$"w"*0.00000001*$"Vmax")
set Voc= $"Voc"

quit
```

Appendix 2: Simulation parameters values

Geometry	
x_{max}	500 µm
y_{max}	220 µm
$w_{electrode}$	50 µm
w_{BSF}	210 µm
w_{BSF+}	90 µm
gap	40 µm
$gap_{electode}$	80 µm
y_{BSF}	1.1 µm
y_{BSF+}	2.3 µm
$y_{emitter}$	5 µm

Doping	
bulkRes	1.4 Ohms.cm
EmitterNPeak	1e19 cm^{-3}
BSFNPeak	0.9e19 cm^{-3}
BSFHighNPeak	6e19 cm^{-3}

Recombination parameters	
tau	10 ms
VEletrode	1e7 $cm.s^{-1}$
SFront (SN = SP)	4 $cm.s^{-1}$
SNBack (gap)	10 $cm.s^{-1}$
SPBack (gap)	5000 $cm.s^{-1}$
SBackBSF	900 $cm.s^{-1}$
SBackBSFHigh	6000 $cm.s^{-1}$
SBackEmitter	8000 $cm.s^{-1}$

Reflectance	
BackReflectance	90 %
FrontReflectance	100 %

Appendix 3: Illumination file for PC1D

The illumination file is presented in the following table. Each line in the file should contain two values, separated by one or more spaces or by a tab. The first is a time, in seconds. The second is an intensity value with units of W/cm2.

0 0.001	49000 0.0425	98000 0.75	147000 11
1000 0.00125	50000 0.045	99000 0.775	148000 11.25
2000 0.0015	51000 0.0475	100000 0.8	149000 11.5
3000 0.00175	52000 0.05	101000 0.825	150000 11.75
4000 0.002	53000 0.0525	102000 0.85	151000 12
5000 0.00225	54000 0.055	103000 0.875	152000 12.25
6000 0.0025	55000 0.0575	104000 0.9	153000 12.5
7000 0.00275	56000 0.06	105000 0.925	154000 12.75
8000 0.003	57000 0.0625	106000 0.95	155000 13
9000 0.00325	58000 0.065	107000 0.975	156000 13.25
10000 0.0035	59000 0.0675	108000 1	157000 13.5
11000 0.00375	60000 0.07	109000 1.5	158000 13.75
12000 0.004	61000 0.0725	110000 1.75	159000 14
13000 0.00425	62000 0.075	111000 2	160000 14.25
14000 0.0045	63000 0.0775	112000 2.25	161000 14.5
15000 0.00475	64000 0.08	113000 2.5	162000 14.75
16000 0.005	65000 0.0825	114000 2.75	163000 15
17000 0.00525	66000 0.085	115000 3	164000 15.25
18000 0.0055	67000 0.0875	116000 3.25	165000 15.5
19000 0.00575	68000 0.09	117000 3.5	166000 15.75
20000 0.006	69000 0.0925	118000 3.75	167000 16
21000 0.00625	70000 0.095	119000 4	168000 16.25
22000 0.0065	71000 0.0975	120000 4.25	169000 16.5
23000 0.00675	72000 0.1	121000 4.5	170000 16.75
24000 0.007	73000 0.125	122000 4.75	171000 17
25000 0.00725	74000 0.15	123000 5	172000 17.25
26000 0.0075	75000 0.175	124000 5.25	173000 17.5
27000 0.00775	76000 0.2	125000 5.5	174000 17.75
28000 0.008	77000 0.225	126000 5.75	175000 18
29000 0.00825	78000 0.25	127000 6	176000 18.25
30000 0.0085	79000 0.275	128000 6.25	177000 18.5
31000 0.00875	80000 0.3	129000 6.5	178000 18.75
32000 0.009	81000 0.325	130000 6.75	179000 19
33000 0.00925	82000 0.35	131000 7	180000 19.25
34000 0.0095	83000 0.375	132000 7.25	181000 19.5
35000 0.00975	84000 0.4	133000 7.5	182000 19.75
36000 0.01	85000 0.425	134000 7.75	183000 20
37000 0.0125	86000 0.45	135000 8	
38000 0.015	87000 0.475	136000 8.25	
39000 0.0175	88000 0.5	137000 8.5	
40000 0.02	89000 0.525	138000 8.75	
41000 0.0225	90000 0.55	139000 9	
42000 0.025	91000 0.575	140000 9.25	
43000 0.0275	92000 0.6	141000 9.5	
44000 0.03	93000 0.625	142000 9.75	
45000 0.0325	94000 0.65	143000 10	
46000 0.035	95000 0.675	144000 10.25	
47000 0.0375	96000 0.7	145000 10.5	
48000 0.04	97000 0.725	146000 10.75	

References

[1] Green, M.A., K. Emery, Y. Hishikawa, W. Warta, and E.D. Dunlop," - Solar cell efficiency tables (version 42)", *Progress in Photovoltaics: research and applications*, Vol. 21, No. 5, 2013, pp. 837.

[2] Repo, P., J. Benick, V. Vähänissi, J. Schön, G. von Gastrow, B. Steinhauser, M.C. Schubert, M. Hermle, and H. Savin," N-type Black Silicon Solar Cells", *Energy Procedia* Vol. 38, No. 0, 2013, pp. 866-871.

[3] Repo, P., A. Haarahiltunen, L. Sainiemi, M. Yli-Koski, H. Talvitie, M.C. Schubert, and H. Savin,"Effective Passivation of Black Silicon Surfaces by Atomic Layer Deposition", IEEE Journal of Photovoltaics, Vol. 3, No. 1, 2013, pp. 94.

[4] Chapin, D.M., C.S. Fuller, and G.L. Pearson," A New Silicon pn Junction Photocell for Converting Solar Radiation into Electrical Power", *Journal of Applied Physics* Vol. 25, No. 5, 1954, pp. 676-677.

[5] Schwartz, R.J., and M.D. Lammert," Silicon solar cells for high concentration applications", Electron Devices Meeting, Vol. 21, 1975, pp.350 - 352.

[6] Cousins, P.J., D.D. Smith, L. Hsin-Chiao, J. Manning, T.D. Dennis, A. Waldhauer, K.E. Wilson, G. Harley, and W.P. Mulligan," Generation 3: Improved performance at lower cost", *Photovoltaic Specialists Conference, IEEE* Vol. 35th, 2010, pp.278.

[7] Schneider, A., L. Rubin, and G. Rubin," Solar Cell Efficiency Improvement by New Metallization Techniques - the Day4 Electrode Concept", *Photovoltaic Energy Conversion, Conference Record of the 2006 IEEE 4th World Conference*, Vol.1, 2006, pp. 1095.

[8] Spath, M., P.C. De Jong, I.J. Bennett, T.P. Visser, and J. Bakker,"A novel module assembly line using back contact solar cells", *Photovoltaic Specialists Conference*, 2008, pp. 1-6.

[9] Granek, F., M. Hermle, C. Reichel, A. Grohe, O. Schultz-Wittmann, and S. Glunz, "Positive effects of front surface field in high-efficiency back-contact back-junction n-type silicon solar cells", PVSC '08. 33rd IEEE, pp.1-5.

[10] Sinton, R.A., and R.M. Swanson, "Simplified backside-contact solar cells", *Electron Devices, IEEE Transactions* Vol. 37, No.2, 1990, pp. 348-352.

[11] Granek, F., "High-Efficiency Back-Contact Back-Junction Silicon Solar Cells", *Fraunhofer Institut für Solare Energiesysteme*, Freiburg im Breisgau: Albert-Ludwigs-Universität, 2009, pp. 209.

[12] McEvoy, A.J., L. Castañer, and T. Markvart *Solar Cells: Materials, Manufacture and Operation*, Second edition ed.: Elsevier, 2012.

[13] Zanuccoli, M., R. De Rose, P. Magnone, E. Sangiorgi, and C. Fiegna, "Performance Analysis of Rear Point Contact Solar Cells by Three-Dimensional Numerical Simulation", *Electron Devices, IEEE Transactions*, Vol. 59, No. 5, 2012, pp. 1311-1319.

[14] Sinton, R.A., Y. Kwark, J.Y. Gan, and R.M. Swanson,"27.5-percent silicon concentrator solar cells", *Electron Device Letters, IEEE* Vol.7, No.10, 1986, pp. 567- 569.

[15] Cousins, P.J., D.D. Smith, L. Hsin-Chiao, J. Manning, T.D. Dennis, A. Waldhauer, K.E. Wilson, G. Harley, and W.P. Mulligan," Generation 3: Improved performance at lower cost", *Photovoltaic Specialists Conference, IEEE* Vol. 35th, 2010, pp.275-278.

[16] Legtenberg, R., H. Jansen, M.d. Boer, and M. Elwenspoek," Anisotropic reactive ion etching of silicon using SF6/02/CHF3 gas mixtures", *Journal of the Electrochemical Society* Vol. 142, No. 6, 1995, pp. 2020-2028.

[17] Elwenspoek, H.J.a.M.d.B.a.R.L.a.M.," The black silicon method: a universal method for determining the parameter setting of a fluorine-based reactive ion etcher in deep silicon trench etching with profile control", *Journal of Micromechanics and Microengineering* Vol. 5, No. 2, 1995, pp. 115.

[18] Jansen, H., M.d. Boer, B. Otter, and M. Elwenspoek, "The black silicon method IV: the fabrication of three dimensional structures in silicon with high aspect ratios for scanning probe microscopy and other applications", *Micro Electro Mechanical Systems, MEMS '95*, Amsterdam, the Netherlands, 1995, pp. 88-93.

[19] Kumaravelu, G., M.M. Alkaisi, and A. Bittar, "Surface texturing for silicon solar cells using reactive ion etching technique", *Photovoltaic Specialists Conference*, 2002, pp. 258-261.

[20] Zaidi, S.H., D.S. Ruby, and J.M. Gee, "Characterization of random reactive ion etched-textured silicon solar cells", *Electron Devices, IEEE Transactions,* Vol.48, No.6, 2001, pp. 1200 - 1206.

[21] Nguyen, K.N., D. Abi-Saab, P. Basset, E. Richalot, F. Marty, D. Angelescu, Y. Leprince-Wang, and T. Bourouina, "Black silicon with sub-percent reflectivity: Influence of the 3D texturization geometry", *Solid-State Sensors, Actuators and Microsystems Conference, 16th*, 2011, pp. 354 - 357.

[22] Dingemans, G., and E. Kessels, "Status and prospects of Al2O3-based surface passivation schemes for silicon solar cells", *Journal of Vacuum Science & Technology A,* Vol.30, No.4, 2012, pp. - 040802-040827.

[23] Frascaroli, J., G. Seguini, E. Cianci, D. Saynova, J. van Roosmalen, and M. Perego, "Surface passivation for ultrathin Al2O3 layers grown at low temperature by thermal atomic layer deposition", *Physica status solidi (a)*, Vol.210, No.4, 2013, pp. 732-736.

[24] SEMI AUX017-0310E; "Contactless carrier-lifetime measurement in silicon wafers, ingots, and blocks", www.semi.org/,2010.

[25] Schroder, Dieter K. *Semiconductor Material and Device Characterization*. 3rd Ed. John Wiley and Sons, Inc. Hoboken, New Jersey, 2006.

[26] Kerr, M.J., and A. Cuevas, "General parameterization of Auger recombination in crystalline silicon", *Journal of Applied Physics* Vol. 91, No. 4, 2002, pp. 2473-2480.

[27] Green, M.A., *Solar Cells: Operating Principles, Technology and System Applications*: Prentice-Hall, 1986.

[28] Pang, S.K., and A. Rohatgi, "Record high recombination lifetime in oxidized magnetic Czochralski silicon", *Applied Physics Letters* Vol. 59, No. 2, 1991, pp. 195-197.

[29] Sinton, R.A., and A. Cuevas, "Contactless determination of current–voltage characteristics and minority carrier lifetimes in semiconductors from quasi‐steady‐state photoconductance data", *Applied Physics Letters* Vol. 69, No. 17, 1996, pp. 2510-2512.

[30] International, S., *Atlas User's Manual DEVICE SIMULATION SOFTWARE*, septembre 2014.

[31] Terlinden, N.M., G. Dingemans, M.C.M. van de Sanden, and W.M.M. Kessels, "Role of field-effect on c-Si surface passivation by ultrathin (2–20 nm) atomic layer deposited Al2O3", *Applied Physics Letters* Vol. 96, No. 11, 2010.

[32] P.P. Altermatt, H. Plagwitz, R. Bock, J. Schmidt, R. Brendel, M.J. Kerr, and A. Cuevas, "The Surface Recombination Velocity at Boron-Doped Emitters: Comparison Between Various Passivation Techniques", *21st European Photovoltaic Solar Energy Conference*, Dresden, Germany, 2006, pp. 647.

[33] Cuevas, A., P.A. Basore, G. Giroult‐Matlakowski, and C. Dubois, "Surface recombination velocity of highly doped n‐type silicon", *Journal of Applied Physics* Vol. 80, No. 6, 1996, pp. 3370-3375.
[34] Müller, J., K. Bothe, S. Gatz, H. Plagwitz, G. Schubert, and R. Brendel, "Recombination at local aluminum-alloyed silicon solar cell base contacts by dynamic infrared lifetime mapping", *Energy Procedia* Vol. 8, No. 0, 2011, pp. 337-342.
[35] Kray, D., M. Hermle, and S.W. Glunz, "Theory and experiments on the back side reflectance of silicon wafer solar cells", *Progress in Photovoltaics: Research and Applications*, Vol.16, No. 1, 2008, pp. 1-15.
[36] Ristow, A., M. Hilali, A. Ebong, and A. Rohatgi, "Screen-Printed Back Contact Reflector For Light Trapping In Crystalline Silicon Solar Cells" *17th European Photovoltaic Solar Energy Conference and Exhibition*; Munich, Germany; October 22-26, 2001.